

The Early Maturity of High-Redshift Galaxies: Insights from sSFR, M/L and SFHs at $z \sim 7 - 14$

P. Santini¹, M. Castellano¹, A. Calabrò¹, A. Fontana¹, E. Merlin¹, D. Bevacqua¹, P. Bergamini², S. Cantarella^{3,4}, L. Ciesla⁵, A. Ferrara⁶, S. L. Finkelstein^{7,8}, F. Fortuni¹, G. Gandolfi¹, T. Gasparetto¹, E. Giallongo¹, N. A. Grogin⁹, S. T. Guida^{1,10,11}, A. M. Koekemoer⁹, N. Menci¹, L. Napolitano¹, D. Paris¹, L. Pentericci¹, B. Perez-Diaz¹, B. Stoyanova^{1,12}, and T. Treu¹³

¹ INAF - Osservatorio Astronomico di Roma, Via di Frascati 33, 00078 Monte Porzio Catone, Italy
e-mail: paola.santini@inaf.it

² INAF - Osservatorio di Astrofisica e Scienza dello Spazio di Bologna, Via Piero Gobetti 93/3, 40129 Bologna, Italy

³ Astronomy Section, Department of Physics, University of Trieste, Via G.B. Tiepolo 11, 34143, Trieste, Italy

⁴ INAF – Astronomical Observatory of Trieste, Via G.B. Tiepolo 11, 34143 Trieste, Italy

⁵ Aix Marseille Univ, CNRS, CNES, LAM, Marseille, France

⁶ Scuola Normale Superiore, Piazza dei Cavalieri 7, 50126 Pisa, Italy

⁷ Department of Astronomy, The University of Texas at Austin, Austin, TX, USA

⁸ Cosmic Frontier Center, The University of Texas at Austin, Austin, TX 78712, USA

⁹ Space Telescope Science Institute, 3700 San Martin Drive, Baltimore, MD 21218, USA

¹⁰ Università di Napoli “Federico II”, C.U. Monte Sant’ Angelo, Via Cinthia, 80126 Napoli, Italy

¹¹ Max-Planck-Institut für extraterrestrische Physik, Gießenbachstraße 1, 85748 Garching, Germany

¹² Physics Department, Tor Vergata University of Rome, Via della Ricerca Scientifica 1, 00133 Rome, Italy

¹³ Department of Physics and Astronomy, University of California, Los Angeles, 430 Portola Plaza, Los Angeles, CA 90095, USA

ABSTRACT

The James Webb Space Telescope (JWST) has revealed an unexpected excess of UV-bright galaxies at $z > 10$, unaccounted for by extrapolations from pre-JWST observations and theoretical models. Understanding the physical properties and star formation histories (SFH) of high redshift systems is key to distinguish between the different proposed scenarios and assess their implications for the galaxy formation and evolution picture. We identify and analyse a sample of 2420 robust candidates at $z \sim 7 - 14$ drawn from the ASTRODEEP-JWST dataset over $\sim 0.2 \text{ deg}^2$ and model their properties with non-parametric SFHs to derive their specific star formation rate (sSFR) and stellar population properties. We find that the median sSFR and M/L remain roughly constant across the probed redshift range. We show that this result is robust against potential systematics unless a hidden population of dust-enshrouded starbursts, undetectable in current data, exists at these redshifts. In any case, the absence of observed high-sSFR systems at the highest redshifts suggests that any dust-free starburst phase must be short-lived. The observed sSFR evolution is in tension with most (though not all) theoretical models, making it a key quantity for discriminating among competing scenarios. The sample shows a wide range of physical conditions and galaxy classes, including systems with low sSFR and high mass-to-light ratios (M/L) up to $z \sim 10$, indicative of already evolved galaxies only a few hundred Myr after the Big Bang, and different degrees of dust attenuation. We finally attempt to reconstruct the assembly histories of two sub-samples, namely a) the highest-M/L galaxies at $z \sim 7 - 8$, which appear to have formed the bulk of their stars at least 500 Myr before observation, implying progenitors observable as UV-bright sources at $z > 20$, and b) the full sample of $z > 11$ galaxies, which formed through stochastic SFH, remaining UV-faint for most of their early evolution, before undergoing recent (~ 50 Myr old) episodes of major growth.

Key words. Galaxies: evolution - Galaxies: formation - Galaxies: high-redshift - Galaxies: star formation - Galaxies: stellar content

1. Introduction

Since the start of science operations, the James Webb Space Telescope (JWST) has immediately demonstrated its revolutionary power for probing the early Universe, especially the first few hundred million years after the Big Bang, pushing the detection frontier to $z \sim 10-15$ (e.g., Castellano et al. 2022; D’Eugenio et al. 2024; Carniani et al. 2024; Napolitano et al. 2025a; Naidu et al. 2025) and possibly beyond (Kokorev et al. 2025a; Pérez-González et al. 2025; Castellano et al. 2025; Gandolfi et al. 2025a,b).

One of the most exciting and consolidated results is the evidence of an unexpectedly high number of rest-frame UV-bright $z \gtrsim 10$ galaxies (e.g., Castellano et al. 2022, 2023; Naidu et al.

2022; Harikane et al. 2023a; Donnan et al. 2023; Finkelstein et al. 2023, 2024; McLeod et al. 2024; Whittler et al. 2025) confirmed by successful spectroscopic follow-up with NIRSpec (e.g., Arrabal Haro et al. 2023; Curtis-Lake et al. 2023; Harikane et al. 2024; Castellano et al. 2024; Carniani et al. 2024; Napolitano et al. 2025a). A very wide range of physical interpretations have been proposed to explain this excess. A first class of models invokes a brightening of the objects due to peculiar star formation (SF) properties, like top-heavy Initial Mass Functions (IMF, e.g., Inayoshi et al. 2022), heavily stochastic SF (e.g., Mason et al. 2023), negligible dust attenuation (e.g., Ferrara et al. 2023; Narayanan et al. 2025). Other models involve an accelerated evolution of galaxies due to enhanced SF efficiency/reduced feed-

back (e.g., Dekel et al. 2023; Somerville et al. 2025; Cantarella et al. 2025), or even an accelerated formation due to potential modifications of the standard cosmological scenario (e.g., Liu & Bromm 2022; Padmanabhan & Loeb 2023; Melia 2023; Menci et al. 2024). The presence of AGNs in high- z galaxies (e.g., Harikane et al. 2023b; Bunker et al. 2023; Castellano et al. 2024; Napolitano et al. 2025b) could also contribute to this excess (Hegde et al. 2024), although several sources responsible for the excess do not show any AGN feature (e.g., Curtis-Lake et al. 2023; Carniani et al. 2024; Napolitano et al. 2025a). The origins of this overabundance are therefore tied to fundamental properties of the high redshift Universe, and motivate the great interest that this problem has raised recently.

Key to discriminate among the proposed scenarios is the investigation of galaxy physical properties and star formation histories (SFH). Thanks to JWST, galaxy physical properties can be measured with significantly larger accuracy than it was possible before (i.e., a factor of 5-10 lower relative uncertainties on the stellar mass, Santini et al. 2023). Furthermore, recent advances in modeling techniques have greatly improved our ability to reconstruct the past SFHs of galaxies (e.g., Leja et al. 2019; Ciesla et al. 2024; Wang et al. 2025a; Carvajal-Bohorquez et al. 2025).

Another surprising result emerging from JWST observations is the remarkable diversity in the physical properties of high redshift ($z > 7$) galaxies. This variety manifests across multiple aspects of galaxy evolution: stellar population properties (e.g., Santini et al. 2023; Conselice et al. 2025; Tang et al. 2025); SFHs (e.g., Dressler et al. 2024; Endsley et al. 2025); quenching timescale, with passive galaxies found very early epochs (e.g., Russell et al. 2025; Weibel et al. 2025; Merlin et al. 2025; Baker et al. 2025); the physical conditions of the interstellar medium in terms of metal abundances, ionization and excitation conditions (e.g., Schaerer et al. 2022; Cameron et al. 2023; Curti et al. 2023; Roberts-Borsani et al. 2025b); structure and morphology (e.g., Kartaltepe et al. 2023; Treu et al. 2023; Lee et al. 2024).

In this paper we focus our attention on the evolution of the specific star formation rate (sSFR), i.e., the SFR per unit stellar mass (M), and on the mass-to-light ratio (M/L_{UV} , M/L in the following), i.e., the ratio between the stellar mass and the rest-frame UV luminosity, which traces the nature of the stellar populations. By combining SF and stellar population properties, we try to reconstruct the assembly history of our galaxies. To achieve this goal we exploit the ASTRODEEP-JWST database (Merlin et al. 2024), consisting of more than 500 thousand sources over an area of 0.2 deg^2 . Assembling a statistically significant galaxy sample is essential to get rid of the (large) uncertainties that may affect individual fits (Wang et al. 2025a).

This paper is organized as follows: we describe the dataset and sample selection in Sect. 2; in Sect. 3 we illustrate the methodology and discuss possible biases and completeness issues; we present our results in Sect. 4 and discuss possible interpretations in Sect. 5; finally, we summarize our findings in Sect. 6. We adopt the Planck18 (Planck Collaboration et al. 2020) Λ CDM cosmology and a Chabrier (2003) IMF. Magnitudes are given in the AB system (Oke & Gunn 1983).

2. Data set

2.1. The ASTRODEEP-JWST catalogs

This work is based on the extensive ASTRODEEP-JWST database publicly released¹ by our group (Merlin et al. 2024).

¹ <http://www.astrodeep.eu/astrodeep-jwst-catalogs/>

It consists of a set of multiwavelength photometric catalogs extracted from eight JWST programs targeting seven distinct areas in the sky. For the ABELL2744 fields we have used data from GLASS-JWST (Treu et al. 2022), UNCOVER (Bezanson et al. 2024), DDT 2756 (P.I. Chen) and GO 3990 (P.I. Morishita); for EGS we exploited the CEERS survey (Finkelstein et al. 2025); JADES (Eisenstein et al. 2023) data have been used for the GOODS-S and GOODS-N fields; a fraction of the Extended CDFS has been mapped by the NGDEEP program (Bagley et al. 2024); finally, the COSMOS and UDS fields have been observed as part of the PRIMER program (GO 1837, P.I. Dunlop).

Photometric catalogs are based on 8 JWST NIRCcam bands (F090W, F115W, F150W, F200W, F277W, F356W, F410M and F444W) and 8 HST bands (ACS F435W, F606W, F775W and F814W, and WFC3 F105W, F125W, F140W and F160W), although not all fields are provided with the full 16 band photometry. Source detection was performed on a weighted stacked F356W and F444W image, and aperture photometry was measured with the A-PHOT software (Merlin et al. 2019) on PSF-matched images. In total, the ASTRODEEP-JWST database contains $\sim 530\text{k}$ sources and covers a sky area of $\sim 0.2 \text{ deg}^2$.

For this work, we used the photometric redshifts estimated with the *zphot* software package (Fontana et al. 2000) and released with the ASTRODEEP-JWST database, as well as the associated probability distribution functions $P(z)$. They were obtained by assuming Bruzual & Charlot (2003) stellar templates, exponentially declining star formation histories, and including nebular emission according to Castellano et al. (2014) and Schaerer & de Barros (2009). When available, we adopted spectroscopic redshifts instead of photometric ones. Indeed, the ASTRODEEP-JWST release also includes ~ 21000 high-quality spectroscopic redshifts available in the literature at the time of release, against which photometric redshifts have been tested. We complemented these with 6031 new high-quality spectroscopic redshifts that have been released in the meantime. They include sources *a*) taken from published works considering the collection of Napolitano et al. (2025a) and Napolitano et al. (2025c) (see references therein), *b*) measured from the NIRSpect GO program 3073 (Castellano et al. in prep.) and *c*) obtained by querying the DAWN JWST Archive (DJA) archive (Heintz et al. 2024; de Graaff et al. 2025), limiting to robust redshifts validated from visual inspection (grade=3). Overall, the photometric redshift accuracy is very good and in line with the standards in the literature, yielding a median $dz = |z_{phot} - z_{spec}| / (1 + z_{phot})$ of 0.006, NMAD² equal to 0.036 and an outlier fraction of 9%, where outliers are defined as sources for which $dz > 0.15$.

We refer the reader to Merlin et al. (2024) for detailed information on photometry, photometric and spectroscopic redshifts.

2.2. Sample selection

To select a robust sample of high redshift ($z \gtrsim 7$) galaxies, we applied a combination of photometry and photo- z criteria, starting from and customising the selection technique presented by Finkelstein et al. (2024) (see also Conselice et al. 2025). We tuned each of the thresholds in the various steps of the selection by checking the performance against spectroscopic sources, aiming at the largest level of completeness keeping a low fraction of low redshift interlopers.

We started by rejecting objects with photometric issues, exploiting the *f*lag columns in the ASTRODEEP-JWST catalogs. In particular, we rejected spurious detections, saturated or

² NMAD=1.48 \times median(dz).

boundary sources, and bad measurements in both the F356W and F444W bands. We also excluded sources missing more than 4 JWST bands, to ensure robust sampling of the spectrum. These cuts reduce the catalogs to $\sim 90\%$ of their parent samples.

We then cut the samples at $\text{SNR} > 5$ in the F444W band, corresponding to $\sim 27.9 - 30.3$ mag, depending on the field ($\sim 62\%$ of the initial dataset).

We considered all sources with redshift higher than 6.5, i.e., $\sim 2.5\%$ of the initial sample, with the exception of COSMOS where the redshift cut selects almost 18% of the sample due to a higher fraction of photo- z failures.

To deal with potential inaccuracies in the photometric redshift estimates and limit the analysis to robust high redshift candidate galaxies, we required detection redward of the Ly α break and undetection blueward of it. In particular, we required *a*) at least three detections redder than F090W/F115W/F150W/F200W, depending on the redshift, of which at least two with $\text{SNR} > 5$, and *b*) at least one measurement shortward of the break and none with $\text{SNR} \geq 2$, considering ACS bands and the three bluest NIRCcam bands, again depending on redshift. This photometric selection results in a further reduction of the samples to 1.5% of the initial number ($\sim 59\%$ of the $z > 6.5$ subsample with reliable photometry, and only 11% for the COSMOS field, compensating the suspiciously large fraction of high redshift sources).

We then applied selections based on the quality of the photometric redshifts, excluding all sources for which the reduced χ^2 of the associated best-fit solution is larger than 10. We required that 70% of the probability lies at $z > 5.5$ and we rejected any source with a secondary redshift solution at $z < 5.5$ whose associated probability is larger than 40% of the best-fit probability. This step of the selection further reduces the samples to 0.5% of the parent catalogs ($\sim 20\%$ of the $z > 6.5$ subsample with reliable photometry, and 3% for COSMOS).

To evaluate the completeness and purity of our sample, we repeated the selections above on the spectroscopic subsample ignoring the spectroscopic redshifts and only relying on photometric ones. In the end, the completeness turns out to be 61% on average (52-76%, depending on the field, its photometric coverage and depth). Roughly half of the low redshift sources incorrectly included in the selection are only slightly below the threshold, not affecting our results appreciably. The fraction of severe interlopers with $z_{\text{spec}} < 5.5$ is 4%. To test whether these objects may affect our results, we run the full analysis described in the following on all known interlopers (with spectroscopic redshift lower than 6.5) which, on the basis of photometric data alone, would be selected by our technique. These sources do not occupy any peculiar region of the diagrams presented in the following, implying that a small fraction of low redshift sources erroneously included in the sample does not impact our conclusions.

Once all selections were applied, we visually inspected all sources and discarded problematic ones not flagged in the parent catalog i.e., defects, spikes, objects whose photometry is clearly affected by noise at the borders of the images or blending issues, and sources with poor fits. Visual inspection removes from a few to up to 11% of objects, depending on the field.

We kept in the sample 275 spectroscopic sources with reliable photometry and SNR in the F444W band larger than 5 which would have been rejected on the basis of photometric and/or photo- z criteria.

Finally, we removed: *a*) known AGN flagged as such in the ASTRODEEP-JWST database (Merlin et al. 2024) or according to the recent literature (see references in Napolitano et al. 2025b); *b*) Little Red Dots, cross-correlating our sample with the lists of

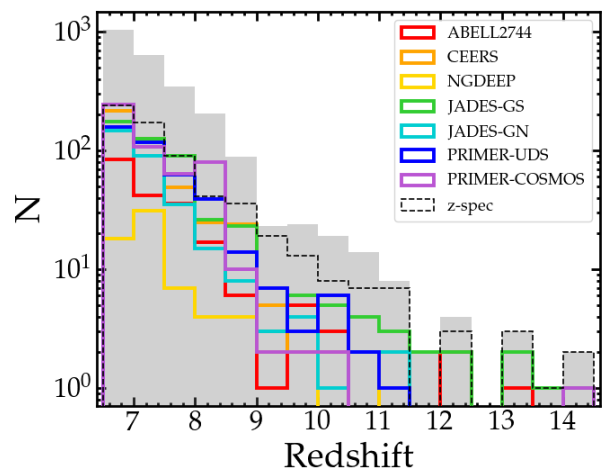


Fig. 1. Redshift distribution of the total sample (gray filled histogram) and of the galaxies selected in the different fields (coloured open histograms, see legend). The black dashed open histogram shows the distribution of spectroscopic sources.

Kokorev et al. (2024), Barro et al. (2024), Pérez-González et al. (2024), Kocevski et al. (2025), and Labbe et al. (2025); *c*) stars, using the SExtractor CLASS_STAR classifier, which is reliable for bright sources, requiring CLASS_STAR > 0.95 & $\text{SNR} > 30$ in detection; *d*) known Brown Dwarfs by considering the lists of Hainline et al. (2024b) and Holwerda et al. (2024). Together, these classes of objects represent 5% of the selected sources.

In total, our sample includes 2420 (53) sources with redshift larger than 6.5 (10), of which 642 (31) are spectroscopic. The redshift distribution in the different fields is shown in Fig. 1.

3. Methods

3.1. Estimate of physical parameters

We estimated physical parameters with the CIGALE SED fitting code (Boquien et al. 2019). We fitted the multiwavelength photometry at fixed redshift and added a 10% relative error in quadrature to flux uncertainties to account for calibration and aperture corrections systematics (Harvey et al. 2025).

Growing evidence suggests that high redshift galaxies have highly stochastic star formation histories (SFH), both based on theoretical arguments (e.g., Muratov et al. 2015; Faucher-Giguère 2018; Furlanetto & Mirocha 2022) and on observational results (e.g., Ciesla et al. 2024; Cole et al. 2025; Endsley et al. 2025; McClymont et al. 2025; Tang et al. 2025; Kokorev et al. 2025b; Carvajal-Bohorquez et al. 2025). For this reason, we modelled our galaxies with flexible non-parametric SFHs, adopting the prescription proposed by Ciesla et al. (2024), shown by the authors to be well suited to high redshift galaxies: the SFH is approximated by a given number of equally, linearly spaced time bins of constant SFR with flat prior, which allows for a high level of stochasticity. The age of the oldest stellar populations can assume 9 values equally spaced from 100 to 900 Myr, never exceeding the age of the Universe at the galaxy redshift. Following Ciesla et al. (2024), we adopted 8 time bins plus a most recent bin of fixed duration t_0 . By definition, t_0 is the timescale over which the SFR is averaged. We adopted $t_0 = 20$ Myr to recover recent short-term SFH variations while avoiding excessive degeneracy, given that photometric data cannot reliably constrain

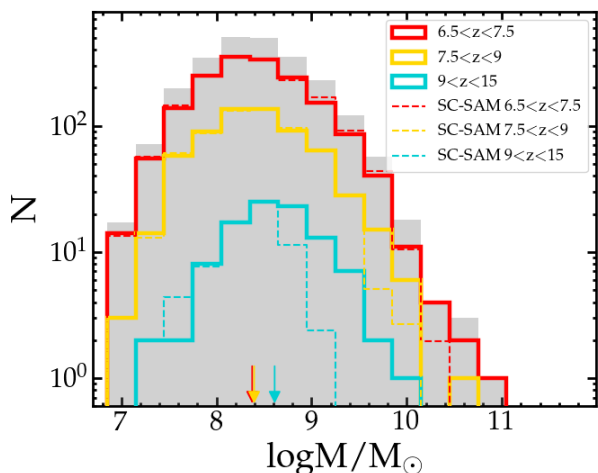


Fig. 2. Stellar mass distribution for the full sample (filled gray) and in three redshift bins (thick solid lines). The small coloured arrows indicate the median of the distribution in each redshift bin. Thin dashed lines show the mass distribution of the Santa Cruz simulation, mass-matched to the observed galaxies (see Sect. 3.3), in the three redshift bins normalized to the peak of the observed mass distributions.

variations of the SED on shorter timescales. Indeed, the fit turns out to be highly degenerate when fixing t_0 to a shorter duration, resulting in extremely large error bars on the SFR.

We adopted the stellar population templates of [Bruzual & Charlot \(2003\)](#), allowing stellar metallicities of 2%, 20% and 100% Solar. Nebular emission was computed using the templates of [Inoue \(2011\)](#) (see [Boquien et al. 2019](#) for details). We set the ionization parameter to $\log U = -3, -2$ or -1 , and allowed gas metallicities of 10%, 20% and 100% Solar. Dust attenuation was modeled with the [Calzetti et al. \(2000\)](#) law ($R_V = 4.05$), with colour excess on the lines $E(B-V)_{\text{line}}$ spanning 0.15–1.7 (9 steps). The colour excess on the continuum, $E(B-V)$, was set to 0.44 times the value on the lines.

Since the physical parameters inferred from the SED fitting analysis might depend on the assumptions, we extensively tested that the overall results of the paper are robust against systematics. We describe in [Appendix A](#) the different fitting setups considered as well as the results obtained.

Physical parameters were inferred as the median of the probability distribution functions (PDF), with uncertainties given by the 16th–84th percentiles. The sSFR and M/L ratios, where L is rest-frame luminosity in the GALEX FUV filter (centered at 1500Å) inferred from the fit, were computed from the PDFs associated with the corresponding quantities for each model.

The ABELL2744 field is a lensed region centered on the galaxy cluster of the same name, and we inferred the intrinsic properties by correcting for magnification using the model of [Bergamini et al. \(2023\)](#). The magnification factors range from ~ 1 to ~ 35 , with a median value of ~ 2 , allowing us to extend the analysis to lower stellar masses than would be possible in the absence of lensing. We note however that sSFRs and M/L ratios, which are the core of this work, are unaffected by lensing.

The mass distribution of our galaxy sample is shown in [Fig. 2](#). The median value is $\log(M/M_\odot) \sim 8.4$ except in the highest redshift bin, where it is equal to ~ 8.6 .

We verified the accuracy of the inferred physical parameters in two ways. We first tested that the SFR agree with those

based on spectroscopy, for the spectroscopic sub-sample. We then checked that the lack of optical constraints for the highest redshift sources does not affect our results, particularly the stellar mass estimates. To this aim, we fitted our sources ignoring the two reddest bands (F410M and F444W). This way, the resulting spectral coverage at $z \sim 8 - 11$ is very similar to that achieved at higher redshifts when the full photometry is used. Despite an increase in the uncertainties, the stellar masses turned out to be ~ 0.1 dex larger on average, producing a similar offset on the sSFR and the M/L at the highest redshifts. This offset is however smaller than the typical statistical uncertainty and well within the dispersion of the sample. A detailed description of these consistency tests can be found in [Appendix B](#).

3.2. Selection window and completeness

Given the complex criteria adopted to select a sample of robust $z \gtrsim 7$ galaxies, we exploit mock galaxies to explore the completeness of our galaxy sample at different masses and luminosities and our ability to recover galaxy properties.

We considered the mock catalogs extracted from the Santa Cruz semi-analytical model (SC-SAM hereafter, [Somerville & Davé 2015; Somerville et al. 2021](#)), and we complemented it with highly obscured ($E(B-V) \geq 0.7$), star-forming galaxies simulated from stellar population synthesis modeling. We perturbed the simulated photometry in order to reproduce the typical photometric uncertainties of our galaxies, we calculated the photometric redshifts and the physical parameters, and we applied the very same selection criteria used on our observed galaxies. The details of the simulation are provided in [Appendix C](#), and the results are shown in [Fig. C.1](#). We briefly summarise them here.

When "standard" galaxies are considered (i.e., from the SC-SAM), the only serious completeness concerns affect low mass ($< 10^8 M_\odot$) and faint ($M_{UV} > -18$) galaxies, as expected, with a completeness of 20-40%. The rest of the sample is instead highly complete, with a level of 70-90% especially in the $10^8 - 10^9 M_\odot$ mass range, i.e. the typical mass of our sources from which we derive the redshift evolution of the sSFR and M/L. The situation is different when heavily dust-obscured ($E(B-V) > 0.7$) sources are examined. Despite some photometric hints ([Rodighiero et al. 2023; Mitsuhashi et al. 2025](#)), their existence at early epochs has not been spectroscopically confirmed yet. However, should they exist, we could not observe them with our data. We would only be able to select 20% of them at $z < 10$, and none at higher redshift. Overall, with the exception of this hypothetical population of high- z extremely dusty galaxies, our technique can properly recover galaxy physical parameters.

3.3. Mass-matched model galaxies

The SC-SAM (see [Appendix C](#) for details) was also taken as a benchmark for comparing our galaxies with model predictions. Since the model is typically characterised by lower mass galaxies than the data sample, for an unbiased comparison we extracted a subset of model galaxies mass-matched to our observations. To this aim, we defined a maximum tolerance in redshift and in mass of $\Delta z = 0.1$ and $\Delta \log M = 0.1$; for each observed galaxy, we picked 10 random simulated galaxies with consistent redshift and stellar mass, avoiding repetitions. For $\sim 13\%$ (7%) of the galaxies, not enough matches were found, essentially due to the lack of simulated massive galaxies at the highest redshifts, so we lowered the redshift and $\log M$ tolerance to 0.2 (0.3). In the

end, only $\sim 2\%$ of the galaxies have no match, basically because the model does not extend to masses larger than $10^{10} M_{\odot}$.

The resulting mass distribution of model galaxies used in our comparisons is shown in Fig. 2.

4. Results

4.1. The evolution of the specific SFR

The redshift evolution of the sSFR is shown in Fig. 3. While the median sSFR is known to increase from the local Universe to $z \sim 6$ (see Santini et al. 2017, and references therein), our results indicate that it remains approximately constant over the previous ~ 600 Myr of cosmic time. This is clear when looking at galaxies with similar mass. The yellow line shows the median trend for $10^8 - 10^9 M_{\odot}$ galaxies (a similar lack of evolution is also observed for lower and higher mass galaxies). In agreement with the median trend, the majority ($\sim 75\%$) of sources have relatively high sSFR ($\sim 20 - 40 \text{ Gyr}^{-1}$). However, we observe notable outliers exhibiting low sSFR up to $z \sim 10$, discussed in Sect. 4.2.

Our measurements show general consistency with previous results, shown by the pink open diamonds, with the exception of the highest values. Part of the mismatch may be ascribed to different assumptions in the estimate of physical parameters, as also shown by the scatter in literature results obtained by different studies for the same sources (open symbols connected by lines in Fig. 3). One key assumption is the SFH, including our choice of a duration of $t_0 = 20$ Myr for the most recent time bin. Averaging over such a timescale smooths out shorter-term variations in star formation (Kim et al. 2025), which cannot be captured by our technique (even though we can measure sSFR up to 60 Gyr^{-1} ; Fig. C.1). In practice, SED fitting integrates emission over timescales that are too long to resolve such rapid events. These variations emerge when adopting a shorter t_0 , such as 10 Myr (setup *b*), Appendix A), at least up to $z \sim 9$. However, even this setup fails to recover extreme sSFR at higher redshift. We cannot exclude that early SFHs may be characterized by even shorter bursts, beyond the reach of our method.

We examined different systematics potentially responsible for the non-evolving sSFR. First, we verified that the overall trend is stable against SED fitting assumptions (Appendix A and Fig. A.1), despite individual galaxies may be strongly affected. Secondly, we considered observational incompleteness. The $10^8 - 10^9 M_{\odot}$ mass range is characterised by a $>90\%$ level completeness at least out to $z \sim 11$ (Sect. 3.2 and Fig. C.1). Additionally, the SC-SAM, which is mass-matched to our sample and thus affected by a similar level of mass incompleteness, shows an increasing trend (dark red dashed line in Fig. 3) that is not seen in our data. We concluded that mass incompleteness cannot explain the flattening, unless a critical population of galaxies with high sSFR is completely missing from both the observed sample and the simulation used to quantify the incompleteness (see Sect. 5.2). Finally, we verified that the lack of optical rest-frame constraints at high redshift can account on average for 0.1 dex (Fig. B.1), which is well within the scatter of the sample and not sufficient to reproduce the increasing trend predicted by most theoretical models and discussed in Sect. 5.1.

4.2. A population of galaxies with low SF activity

Remarkably, we observe a population of galaxies hosting very low star formation activity up to very early cosmic epochs ($z \sim 10$). They are characterized by low SFR ($\lesssim 3 M_{\odot}/\text{yr}$, but typi-

cally < 0.5), masses at the high end of the distribution (mostly $\log(M/M_{\odot}) > 9$), and show a wide range of dust attenuation.

The presence of quiescent galaxies at the redshifts probed by our analysis has already been reported by previous works by means of dedicated photometric searches (e.g., Russell et al. 2025; Merlin et al. 2025; Baker et al. 2025) as well as spectroscopic confirmations ($z \sim 7.3$, Looser et al. 2024; Weibel et al. 2025). We compared the most extreme ones (14 galaxies, with sSFR lower than 0.1 Gyr^{-1}) with our previous analysis (Merlin et al. 2025), where we identified 12 candidates at $z > 6.5$ with $\log(M/M_{\odot}) > 9.5$ adopting different SED fitting and selection technique. Six of the candidates from the present study have negligible (4 sources) or very low sSFR ($\sim 0.15 - 0.25 \text{ Gyr}^{-1}$, 2 sources) in Merlin et al. (2025), including an object at $z \sim 10.2$, but did not eventually pass the final, conservative selection (in some cases only because below the chosen mass limit). The two spectroscopically confirmed quiescent galaxies by Weibel et al. (2025) and Looser et al. (2024) are still quiescent, but just above the chosen threshold in the present work (sSFR ~ 0.1 and 0.4 Gyr^{-1}). Finally, among our candidates with low sSFR, are object that are fitted as star-forming galaxies by Merlin et al. (2025), which highlights how sensitive the results are to the selection criteria used to identify this class of galaxies.

While a detailed analysis of these candidates and investigation of differences among various selection techniques are beyond the scope of the present paper, our findings are in broad agreement with a scenario where a fraction of massive galaxies quench at early times. This illustrates the variety of SF conditions already in place as early as $z \sim 10$.

4.3. The mass-luminosity relation

We explore here the stellar content of our galaxies by looking at the relation between the stellar mass and the rest-frame UV luminosity in three redshift bins, shown in Fig. 4. Thanks to the large dataset, spanning a wide sky area and probing low luminosities, our sample extends beyond previous analyses, covering five magnitudes in luminosity and over three dex in stellar mass.

We do observe a moderate-to-high correlation between the stellar mass and the absolute magnitude (Pearson coefficient between -0.5 and -0.7 , $p\text{-value} \ll 0.001$), and fit a mass-luminosity relation which is consistent with no evolution over the redshift range probed by the present work, as shown by the best-fit parameters reported in Table D.1. We note that, while the relation between mass and UV luminosity has been shown for spectroscopic $z = 9 - 14$ galaxies by Tang et al. (2025), to our knowledge this is the first attempt to derive a best-fit at these redshifts.

The scatter around the relation is very large: for a given luminosity, the bulk of the population spans one order of magnitude in stellar mass, but individual galaxies can vary by more than a factor of 100, reflecting a large variation in the stellar population properties. For this reason, we warn against the use of the UV luminosity as a tracer of the stellar mass, a common practise until the advent of JWST due to the lack of IR constraints (see extended discussion in Santini et al. 2023).

We compared our results with previous works. We first considered our previous analysis (Santini et al. 2023), where we observed no correlation between the stellar mass and the luminosity. This was likely a consequence of the small number statistics affecting the very first JWST data, only probing a limited range in luminosity. Additionally, our previous results were likely prone to the outshining effect, known to lead to underestimated stellar masses (Papovich et al. 2001; Leja et al. 2022). Indeed, we now infer larger masses at $z > 7.5$ due to the adoption

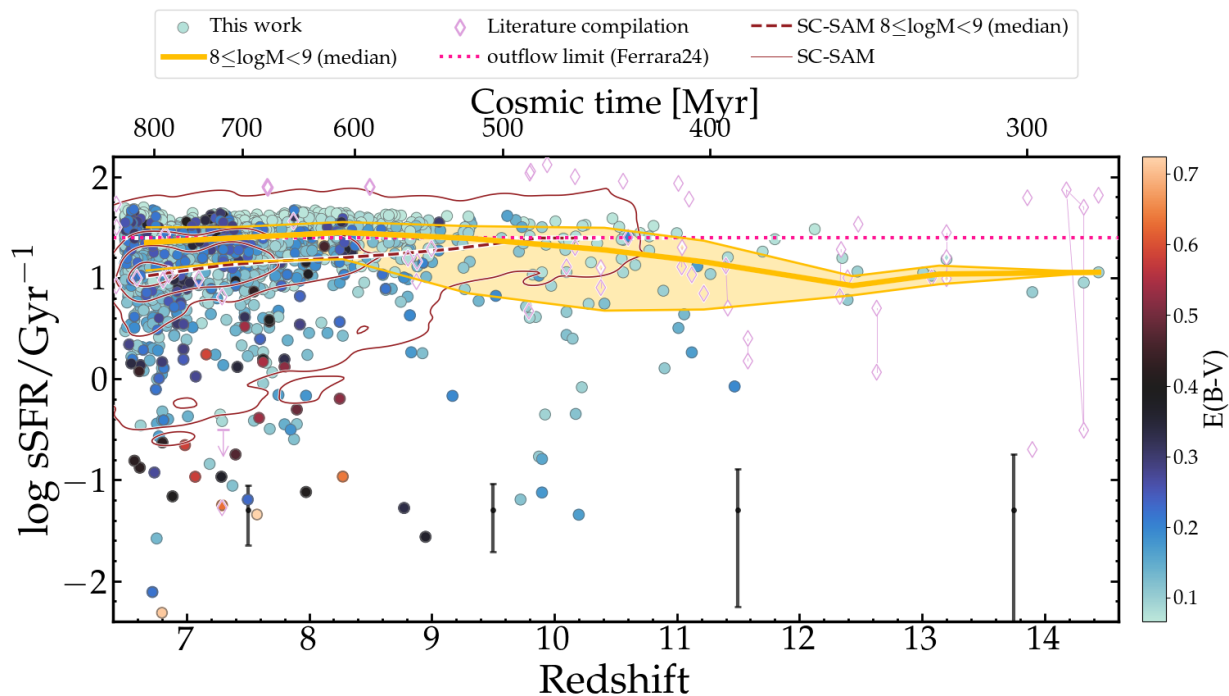


Fig. 3. Evolution of the sSFR. The median error bar in bins of redshift is shown at the bottom. The yellow line and shaded region represent the median and 16th-84th percentile range of the $\log(M/M_{\odot}) = 8 - 9$ subsample. Points are colour-coded according to the dust attenuation $E(B-V)$. Being the $E(B-V)$ calculated on a discrete grid, for visualization purposes we adopt the likelihood-weighted average. Pink open diamonds show a compilation of spectroscopic, JWST-based results taken from the recent literature (Tacchella et al. 2023; Robertson et al. 2023; Roberts-Borsani et al. 2023; Arrabal Haro et al. 2023; Wang et al. 2023; Zavala et al. 2025; D’Eugenio et al. 2024; Hsiao et al. 2024; Hainline et al. 2024a; Harikane et al. 2024, 2025; Looser et al. 2024; Carniani et al. 2024, 2025; Topping et al. 2025; Trussler et al. 2025; Álvarez-Márquez et al. 2025; Helton et al. 2025b; Wu et al. 2025; Naidu et al. 2025; Witstok et al. 2025; Kokorev et al. 2025b; Donnan et al. 2025; Weibel et al. 2025), with lines connecting different estimates for the same sources. Where available, we considered the SFR averaged over a timescale which is as close as possible to our choice of 20 Myr, sometimes averaging estimates over different timescales. The magenta horizontal dotted line represents the sSFR threshold for developing radiation driven outflows capable of expelling dust according to the model of Ferrara (2024a) (see text). The dark red dashed line and solid thin curves are the median and 10%, 50%, 80% and 99.9% probability densities for the SC-SAM.

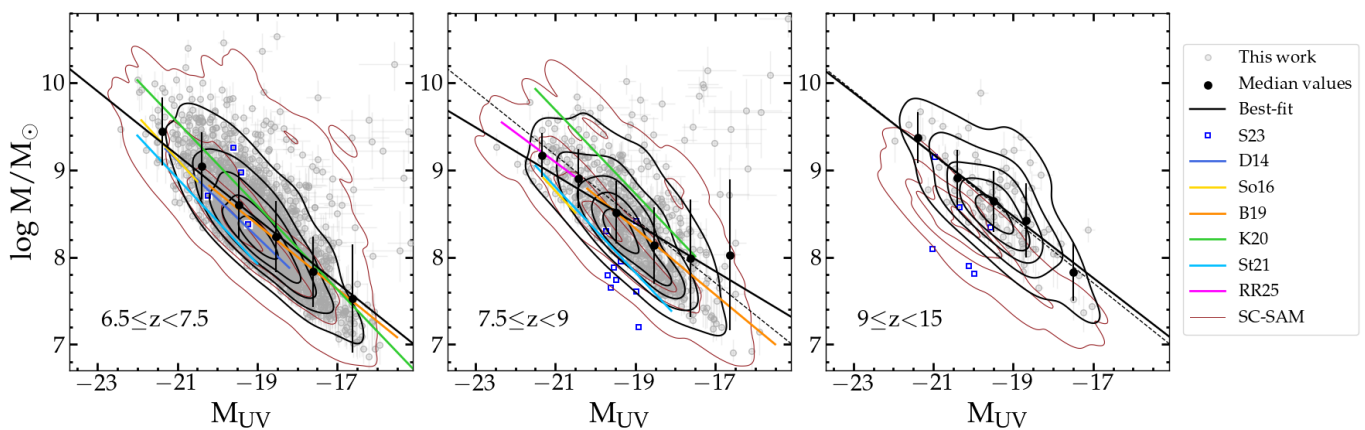


Fig. 4. Relation between the stellar mass and the rest-frame UV absolute magnitude in three redshift bins. Thin black lines enclose 10%, 30%, 50%, 70%, and 90% probability densities. Large black symbols represent the median mass and 16th-84th percentile range in bins of absolute magnitude. The black line shows the best-fit relation, and the dashed lines replicate the best-fit at $z \sim 7$ in the other redshift bins. Coloured lines and symbols illustrate previous results in the literature: Duncan et al. (2014, D14), Song et al. (2016, So16), Bhatawdekar et al. (2019, B19), Kikuchihara et al. (2020, K20), Stefanon et al. (2021, St21), Santini et al. (2023, S23), Rojas-Ruiz et al. (2025, RR25). The dark red thin curves enclose 10%, 50%, 80% and 99.9% probability densities for the SC-SAM.

of more flexible SFHs, which include the possibility of a recent burst to reproduce the UV light (either through bins of constant star formation in the non-parametric fits, or through an exponen-

tial burst or a constant value prior to the observation for parametric SFHs). Moreover, thanks to the possibility of explaining the UV light with a recent burst of star formation, we could fix

the minimum age of the oldest stellar populations to 100 Myr instead of 10 Myr, which in our previous analysis was responsible for the very low mass measurements. At $z \sim 8$, our best-fit relation nicely agrees with the estimate of Rojas-Ruiz et al. (2025), derived from bright BoRG-JWST (Roberts-Borsani et al. 2025a) galaxies. Our results also overlap with those from Bhatwadekar et al. (2019), based on deep HST photometry in the Hubble Frontier Fields and extending to low masses and luminosities. However, compared to other pre-JWST works, the best-fit relation is offset in both directions (with Stefanon et al. 2021, Duncan et al. 2014 and Song et al. 2016 finding a lower normalization and Kikuchihara et al. 2020 a larger one), with the offset being more pronounced at $z \sim 8$ than at $z \sim 7$. This highlights the importance of deep, rest-frame near-IR photometry for estimating accurate stellar masses at high redshift.

We also compared our results with the mass-matched SC-SAM. At $z < 9$ the data are well reproduced, with the exception of the most extreme sources with large stellar masses and faint luminosities. In both redshift bins, the inferred mass–luminosity relation agrees with the observed one at $z \sim 7$. At $z > 9$, however, it is lower by a factor of ~ 3 , with the SC-SAM predicting brighter luminosities for a given stellar mass (we note, however, that the simulation nearly lacks sources with $M \gtrsim 10^9 M_\odot$ at these redshifts). One possible explanation for this finding is the absence of dust reddening in the SC-SAM at $z \gtrsim 10$. In summary, the comparison suggests that the model is unable to reproduce the full variety of galaxies, as discussed in the next section.

4.4. The diversity of the stellar populations

We finally focused on the mass-to-light ratio, which is a proxy of the stellar populations hosted by the galaxy. In Fig. 5 we report the redshift evolution of M/L . As discussed in Sect. 4.3, we derive larger M/L compared to our previous work thanks to mitigation of the outshining effect on the inferred stellar masses.

For a given redshift, our sample spans up to four orders of magnitude in M/L at $z \sim 7$ and roughly a factor of 50 at $z \sim 10$, irrespective of the fitting setup (see Fig. A.1). We note that spectroscopic sources span the whole distribution, indicating that potential photometric redshift degeneracies do not impact our conclusions.

Notably, we observe high M/L ratios up to $z \sim 10$. In principle, a high M/L indicates the presence of evolved stellar populations, although dust attenuation can increase the observed value even in young, star-forming galaxies. High- M/L sources have large stellar masses ($\log(M/M_\odot) \gtrsim 9$) and are typically heavily attenuated ($E(B-V) > 0.3$). They however have ages larger than 350 Myr, occupying the high-age tail of the distribution. Unsurprisingly, a fraction (26%) of the most extreme ones (23 sources with $\log(M/L) > -18$, where M/L is expressed in units of $M_\odot/(\text{erg s}^{-1} \text{Hz}^{-1})$) overlap with the population of quiescent galaxies discussed in Sect. 4.2. The remainder have sSFR typically below $\sim 1/\text{Gyr}$, with only two sources exceeding $2/\text{Gyr}$. Although some may still be forming stars at a moderate rate, these galaxies have already assembled a large stellar mass and likely host evolved stellar populations. Conversely, roughly half of the most extreme quiescent systems have $\log(M/L)$ between -18 and -19 (in the same units) and low dust attenuation ($E(B-V) < 0.3$), suggesting that they recently stopped forming stars and still retain light from comparatively younger stars.

These results indicate that the high-redshift galaxy population is largely diverse, as also suggested by the scatter around the mass-luminosity relation. Galaxies are observed at different evolutionary stages, and their diversity reflects a wide range of

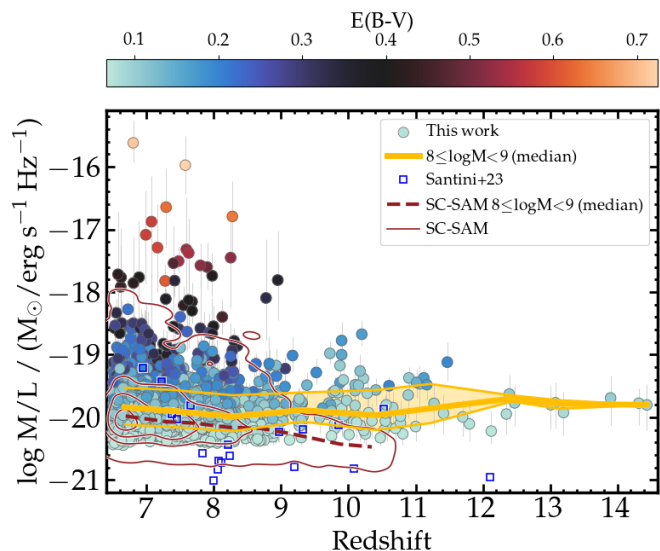


Fig. 5. Evolution of the M/L , where L is the rest-frame UV luminosity. Points are colour-coded according to the dust attenuation $E(B-V)$. The thick yellow line indicate the median of the $\log(M/M_\odot) = 8 - 9$ subsample and the shaded region spans the $16^{\text{th}}-84^{\text{th}}$ percentile range. The dark red dashed line and solid thin curves are the median and 10%, 50%, 80% and 99.9% probability densities for the SC-SAM.

star formation histories and dust attenuation, as indicated by the colour-coding of Fig. 3 and 5. In particular, we can identify distinct galaxy classes: *a*) star-forming sources with moderate level of dust attenuation ($E(B-V) < 0.2$) and young stellar populations, covering the full redshift range and accounting for $\sim 75\%$ of the sample; *b*) more dusty ($E(B-V) \sim 0.2 - 0.7$) star-forming galaxies at $z \lesssim 9 - 10$; *c*) galaxies with low sSFR spanning the whole $E(B-V)$ range ($\sim 0.1 - 0.7$) and characterized by intermediate to large M/L . The observed variety in early galaxy properties confirms with much larger statistics the results obtained by our previous analysis (Santini et al. 2023) as well as by other studies in the literature (e.g., Dressler et al. 2024; Conselice et al. 2025; Tang et al. 2025).

As discussed in Sect. 4.3, the diversity observed in galaxy stellar populations is not fully reproduced by theoretical simulations, which struggle to produce high M/L and evolved stellar populations at high redshift (see Merlin et al. 2025, and references therein), especially at $z > 9$. This likely reflects the smooth, monotonic SFHs in SAMs (Côté et al. 2018): the lack of intense bursts or rapid growth phases reduces the scatter in M/L and hampers the formation of relatively evolved stellar populations at early times.

Even though galaxies with high M/L ratios become rarer and rarer at earlier times, as expected, the median observed M/L calculated on $10^8 - 10^9 M_\odot$ galaxies does not show any redshift evolution. While mass incompleteness may play a role, this cannot entirely explain the observed trend for two reasons. First, we have shown that the level of completeness is very high in that mass range (see Sect. 3.2). Secondly, as discussed in Sect. 4.1, mock galaxies extracted from the SC-SAM show a decreasing trend despite being mass-matched to our sample and therefore suffering from a similar level of mass incompleteness. Finally, the observed flat M/L cannot be explained by SED fitting systematics, as different fitting setups provide the same picture (see Appendix A and Fig. A.1) nor by the lack of optical constraints at $z > 10$ (Appendix B and Fig. B.1).

5. Discussion

We attempt here to interpret our findings by comparing them with theoretical predictions and exploring how galaxies have assembled their mass. Before proceeding, we stress that our conclusions on the galaxy progenitors and their observability entirely stands on the ability to correctly recover galaxy SFHs, known to be an extremely challenging task (e.g., Haskell et al. 2024; Wang et al. 2025a; Carvajal-Bohorquez et al. 2025). We also note that we considered the best-fit SFHs, whose associated properties may slightly vary compared to the median values adopted in this work, and assume that each galaxy derive from one single progenitor.

5.1. The theoretical framework

Since the first JWST results appeared, theoretical models have struggled to reproduce the many unexpected findings, the most established one being the excess of UV-bright galaxies at $z \gtrsim 10$. Different models have implemented different prescriptions to address this issue. As detailed in the introduction, three main classes of interpretations can be identified: models boosting the UV luminosity, models enhancing the star formation efficiency, and models invoking a change in the cosmological paradigm responsible for accelerating galaxy growth, as suggested by recent DESI results (Adame et al. 2025). We compare here the observed evolution of the sSFR with examples from each class above.

We first considered the Attenuation Free Model (AFM hereafter) of Ferrara et al. (2023). It explains the excess of UV luminosity by reducing dust attenuation through radiation-driven outflows that efficiently expel dust from early galaxies, enhancing visibility. These outflows are developed once the galaxy luminosity becomes super-Eddington, i.e., once galaxies exceed a given threshold in sSFR (Ferrara 2024a).

We then considered two variants (Cantarella et al. 2025) of the GAEA semi-analytical model (De Lucia et al. 2024) aimed at enhancing star formation by suppressing the feedback. The first one is the ‘feedback-free starburst’ (FFB) model, inspired by Dekel et al. (2023), combined with a weakened feedback. In this variant, the star formation efficiency at $z > 10$ is increased by shortening the free-fall time to 10 Myr, below the time required for stars to develop winds and supernovae. In addition, the stellar feedback is reduced at $z > 4$ (see Cantarella et al. 2025 for detail). The second model variant is the ‘no high- z stellar feedback’ one, in which the stellar feedback is suppressed at $z > 10$ by shutting down gas reheating and energy injection.

Finally, we examined the framework developed by Menci et al. (2024) to test the effect of assuming a Dark Energy with negative cosmological constant Λ . A negative Λ boosts the dark matter halo masses at high redshift with respect to the Λ CDM scenario ($\Lambda = 0.7$), therefore naturally produces larger stellar masses and higher luminosities, which are obtained by standard assumptions and maximizing the SF activity. To highlight this effect, we considered the extreme case of $\Lambda = -2$.

In Fig. 6 we show the predicted redshift evolution of the sSFR according to the models described above, compared to the observed evolution of $8 \leq \log(M/M_\odot) < 9$ galaxies.

According to the AFM, the sSFR increases with redshift as $(1+z)^{3/2}$ (magenta line in Fig. 6, see also the similar trend $\propto (1+z)^{2.25}$ predicted by Dekel et al. 2013; Davé et al. 2011). A similar behaviour is shown by the fiducial GAEA model (black line and shaded region) and by the framework developed by Menci et al. (2024) (dark and light green dash-dot curves). In the latter case, a negative Λ only results in a slightly larger normal-

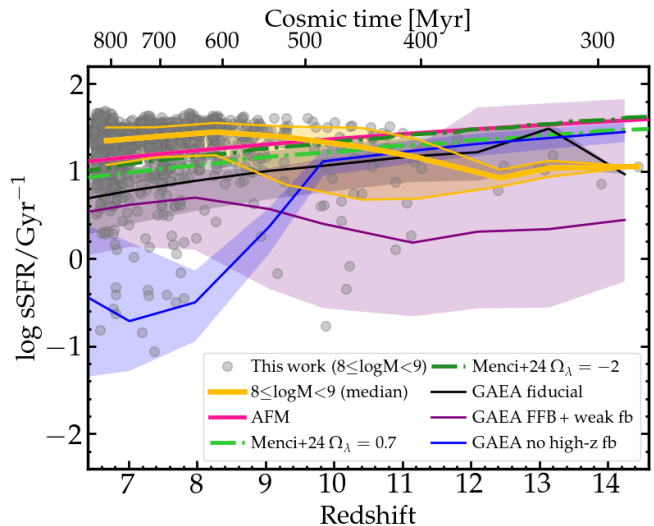


Fig. 6. Evolution of the sSFR. Gray symbols are the observed galaxies in the $10^8 - 10^9 M_\odot$ mass range, and the yellow line and shaded region indicate the median and 16th-84th percentile range. The magenta line shows the prediction of the AFM model of Ferrara (2024a). The dash-dot light and dark green curves are the expectation of the framework outlined by Menci et al. (2024) for $\Lambda = 0.7$ and $\Lambda = -2$, respectively. We show in black, purple and blue the expectation of the GAEA fiducial model, ‘FFB + weak feedback’ and ‘no high- z feedback’ variants, respectively, with solid lines and shaded regions representing the median and the 16th-84th percentile range of $10^8 - 10^9 M_\odot$ model galaxies.

ization, implying that it boosts both SFRs and stellar masses in a rather similar way. All these trends are in contrast with the lack of evolution shown by the observed galaxies. Interestingly, the two GAEA model variants exhibit opposite behaviours, as also highlighted by the authors (see Cantarella et al. 2025, and their Fig. 11), due to the combined effect of free-fall time and feedback, responsible for gas consumption and depleting, respectively. In the ‘FBB + weak feedback’ model, the gas reservoir is rapidly converted into stars at early times³ in a bursty mode, leading to a milder star formation activity at the redshifts probed in this work. The latter is sustained over time by the weak feedback, which prevents extremely high sSFR and at the same time a too early gas consumption. Although roughly 0.7 dex lower in normalization and unable to reproduce galaxies with high sSFR at $z \lesssim 9$, only this model variant depicts a redshift evolution which is similar to the observed one. We note that it also reproduces the quiescent galaxies when the full 3σ distribution is considered (see also Dekel et al. 2025). In contrast, in the ‘no high- z stellar feedback’ scenario the gas amount is larger at early epochs, leading to a larger SFR, which is suppressed at later times ($z < 10$) when feedback becomes effective. While this scenario is capable of reproducing the observed $z \gtrsim 10$ galaxies and sources with low sSFR at $z \sim 7 - 8$, it does not reproduce the bulk of the population at $z < 9$. A similar result is found by Cantarella et al. (2025), who demonstrate how this model variant is in contrast with recent works presenting the Main Sequence at $z \sim 7 - 8$ (Leethochawalit et al. 2023; Cole et al. 2025).

The overall theoretical picture remains unclear. Despite several mechanisms have been proposed to match the observed $z > 10$ luminosity functions, yet none appears able to reproduce the full diversity of galaxies, suggesting that there is no

³ Star formation starts at $z \sim 15 - 20$ in the GAEA model.

single explanation and that a combination of physical processes is likely at play. In this context, the sSFR seems to be a powerful key quantity to discriminate among the various interpretations, with different models predicting different evolutionary trends. However, in order to use the observed sSFR evolution as a benchmark, we need to exclude any possible observational bias affecting our results.

5.2. Are we missing a substantial population of starbursting galaxies?

As shown by the comparison with model predictions (Sect. 5.1), assessing the evolution of the sSFR is crucial to understand the physical mechanisms regulating the formation and evolution of the first galaxies. The observed median sSFR and M/L show no evolution over ~ 600 Myr of cosmic time. Is this the true evolution - at odds with most models except the ‘FFB + weak feedback’ scenario implemented in the GAEA simulation (Cantarella et al. 2025) - or does our dataset miss a population of highly star-forming galaxies at high redshift? If such galaxies exist, they would have high sSFR and young stellar populations, and thus low M/L. Their absence from our sample would push the median sSFR (M/L) toward lower (higher) values, potentially explaining the mismatch between the observed redshift evolution and that predicted by most models.

In Sect. 3.2 we have tested our sensitivity to a potential population of starbursting, extremely dust-enshrouded sources at early epochs. As discussed above and shown in the right panels of Fig. C.1, our selection technique is unable to include dusty galaxies at $z > 10$, so we cannot exclude their existence. As a matter of fact, none of the $z > 9$ (11.5) galaxies in our sample are fitted with $E(B-V)$ larger than 0.2 (0.1), at variance with $z < 9$ sources, where a small fraction of objects shows moderate or high levels of dust obscuration (up to $E(B-V) \sim 0.7$, see Fig. 3 and 5). Indeed, the lack of optical constraints at high redshift makes the selection more prone to dust obscuration issues. Indications of moderately to highly obscured candidates at $z \sim 11 - 12$ has been provided by previous works (Rodighiero et al. 2023; Mitsuhashi et al. 2025), suggesting that dusty galaxies may indeed exist at such early epochs.

The existence of a dusty, starbursting galaxy population has been postulated within the framework of the AFM (Ferrara 2024a). According to this model, at $z \sim 10$ the typical sSFR exceeds a critical value (shown by the dotted magenta horizontal line on Fig. 3) above which galaxies develop the outflow capable of heating and expelling dust and gas. This super-Eddington outflow phase, dubbed blue monster phase, is preceded by an intense, highly dust-obscured phase of star formation, during which 70% of stars are formed, claimed to be unobservable with JWST due to extreme attenuation (Ferrara 2024b). In this context, given the outcome of our simulation (Sect. 3.2 and Appendix C), extremely dusty galaxies would be missed, and the only star-forming phase accessible to our study would therefore be the dust-free, blue monster phase. The fact that none of the galaxies at $z \gtrsim 12$ is in or close to the super-Eddington regime (i.e., above the given threshold in sSFR), implies that the duty cycle of the blue monster phase at these early epochs must be shorter than 10–20 Myr⁴, hence shorter than the ~ 40 Myr predicted by Ferrara (2024b) for the case of GS-z14-0 (Carniani et al. 2024). The short duty cycle, combined with limited statistics at extreme redshifts, may determine our failure in capturing

galaxies in the dust-free phase following the outflow and preceding the SF suppression due to gas removal.

5.3. The assembly history of the highest redshift galaxies

Although we cannot directly probe the existence of $z > 10$ dust-obscured galaxies with current data, we can test the hypothesis that the highest redshift sources in our sample result from the suppression of star formation in galaxies that have recently undergone an intense star-forming phase.

To this aim, we traced back the SFH reconstructed from SED fitting to assess whether these galaxies experienced a higher SF in their recent past. We calculated their mass assembly history, accounting for the recycle fraction, and thus derived their sSFR histories (sSFHs). Peaks in the sSFH correspond to phases of major mass assembly.

For the sake of clarity, we limited the analysis to the most distant sources at $z > 11$ (19 sources - a similar scenario is obtained when considering all $z > 10$ galaxies), and show the results in the left panel of Fig. 7. Their SFHs and sSFHs are variegated and show ups and downs, similar to the so-called lulling or breathing galaxies (e.g., Looser et al. 2025; Gelli et al. 2025; Merlin et al. 2025). Fourteen of these galaxies (74%) have experienced a phase of intense growth - and had a sSFR above the magenta dotted line - over their past $\lesssim 50$ Myr, populating the super-Eddington regime for short, repeated episodes during that time. This fraction is consistent with the fraction of super-Eddington galaxies predicted by the AFM at these redshifts, i.e. ~ 0.5 at $z \sim 11$ and ~ 0.75 at $z \sim 14$ (Ferrara 2024a), qualitatively in agreement with the scenario depicted by the model. The remaining five galaxies have SFH peaking at $z \sim 20 - 40$, and have not been experiencing super-Eddington sSFR since $z \sim 20 - 30$. The entire sample of $z > 11$ galaxies were formed and have assembled their full mass over their past 150-300 Myr, indicating that we are witnessing the process of formation of these systems.

By making reasonable assumptions, it is possible to assess the observability of the progenitors of the highest redshift galaxies. Starting from the SFH, we estimated the UV luminosity as a function of cosmic time by converting the SFR through the typical SFR-to-UV luminosity ratio (K_{UV}^{obs}) observed for our dataset. As expected, K_{UV}^{obs} is correlated with dust attenuation, with larger values observed for higher levels of obscuration. The values of $\log K_{UV}^{obs}$ span 3 dex, but 85% of the sample lies between -27.8 and $-27.1 M_{\odot} \text{yr}^{-1} / (\text{erg s}^{-1} \text{Hz}^{-1})$, with the distribution peaking at -27.7 . At the highest redshift ($z \gtrsim 12$), where we are interested in reconstructing the UV luminosity, the distribution of $\log K_{UV}^{obs}$ is much narrower and limited to the range between -27.7 and -27.85 . As a first approximation, we adopted $\log K_{UV}^{obs} = -27.7$, keeping in mind that a 0.4 dex change in $\log K_{UV}^{obs}$ reflects into a change in the UV luminosity of 1 magnitude.

The resulting luminosities at different times are shown in the second row panels of Fig. 7 (left panels). The progenitors of the highest-redshift sources typically have faint UV luminosities. Only $\sim 20\%$ of galaxies are brighter than a magnitude of -20 (the threshold for "bright" objects, i.e., more or less the "knee" of the luminosity function, Finkelstein et al. 2024) beyond $z \sim 15 - 20$, and only $\sim 35\%$ exceed -17 , which is the expected faint-end limit the search can reach (Pérez-González et al. 2025). Overall, the majority of the progenitors of the highest redshift galaxies are expected to remain hidden to our view even without the need of an extremely dust obscured phase. We note that the fraction of observable sources would further decrease in case of high dust attenuation.

⁴ A similar result is obtained when adopting $t_0 = 10$ Myr; see setup b) in Appendix A.

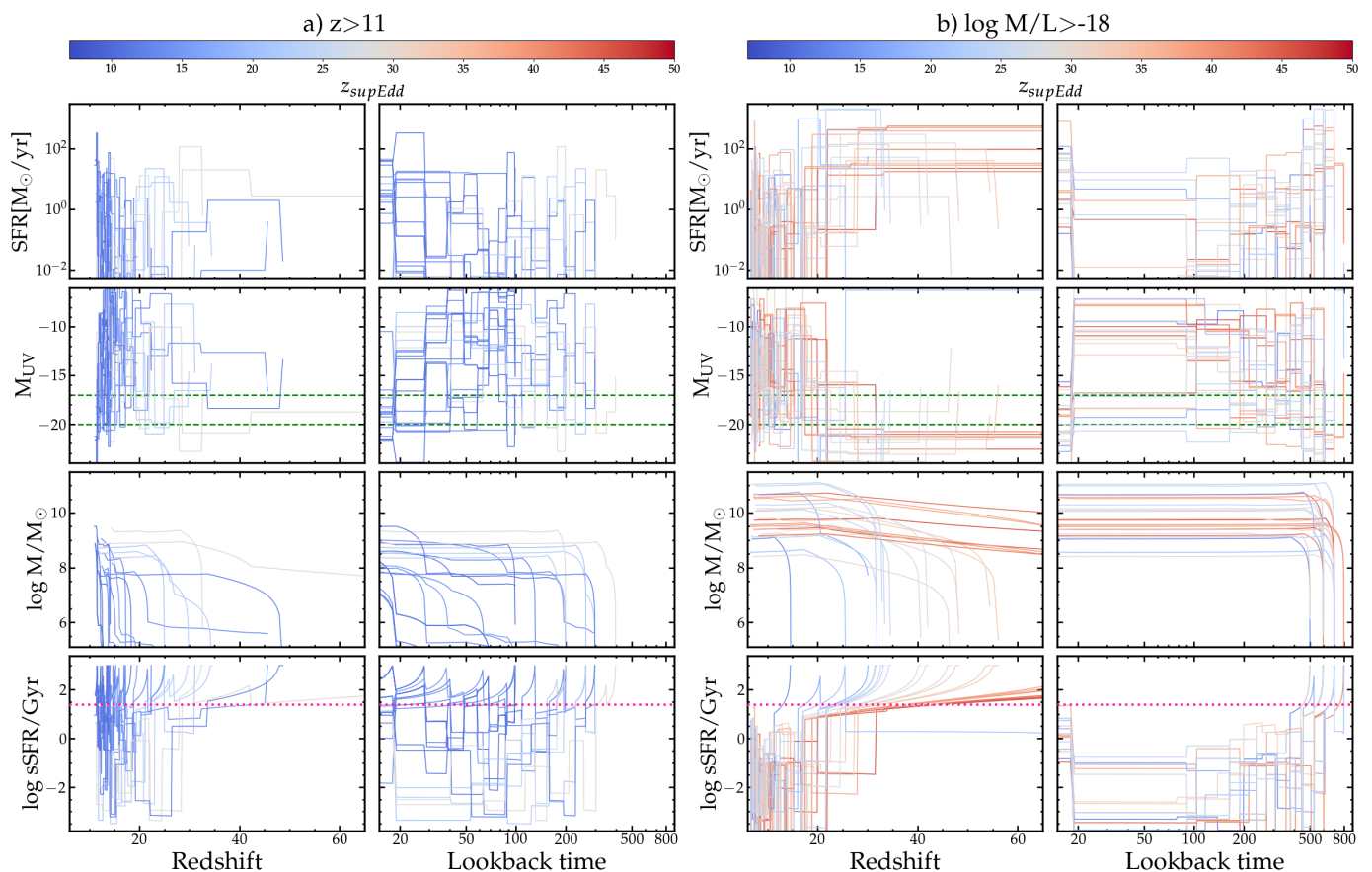


Fig. 7. Panel *a*) SFR (top), UV absolute magnitude (2nd row), stellar mass (3rd row) and sSFR (bottom) as a function of redshift (left) and lookback time (right) of $z > 11$ galaxies. Panel *b*) Same as panel *a*) but for $\log(M/L)/(M_{\odot}/(\text{erg s}^{-1}\text{Hz}^{-1})) > -18$ galaxies, mostly concentrated between $z \sim 7$ and $z \sim 8$. Tracks are colour-coded according to the redshift when they last crossed the outflow threshold, shown by the horizontal magenta dotted line: in the context of the AFM, the sources shown in blue have recently experienced a phase of elevated sSFR, while red ones are in the sub-Eddington phase since $z \sim 30$ at least. Green lines in the 2nd row panels show the depth limits in UV absolute magnitude of -17 and -20.

In summary, within the framework outlined by the AFM, our data are consistent with a scenario in which we are observing the highest redshift galaxies shortly after the onset of radiation-driven outflows and at the conclusion of a dust-enshrouded star formation episode, in a phase of more moderate activity. The most intense phases of formation of these galaxies cannot be observed with the available data. Similar conclusions on the past history of high redshift galaxies have been proposed by Dressler et al. (2024) to explain the lack of sources with increasing SFH as recovered by SED fitting, and by Nakazato & Ferrara (2024) based on theoretical arguments.

5.4. The progenitors and assembly of evolved galaxies

Here we focus our attention on another peculiar subclass of galaxies, i.e. those galaxies that show high M/L within the first few hundreds Myr after the Big Bang. Again, we limit the analysis to the most extreme sources, showing those with the highest M/L, i.e., $\log(M/L) > -18$, where M/L is expressed in units of $M_{\odot}/(\text{erg s}^{-1}\text{Hz}^{-1})$, mostly observed at $z \sim 7-8$. We explore their assembly histories and make predictions on the observability of their progenitors at different cosmic times. We show the results in the right panels of Fig. 7.

The vast majority of these galaxies formed the bulk of their stars 500–800 Myr before observation, i.e. at $z \gtrsim 20-30$. By $z \sim 11-14$ they had already assembled (most of) their final

stellar mass, exceeding the masses of the galaxies observed at those redshifts, which therefore are unlikely to be their progenitors. Galaxies with high M/L experienced intense SF activity in their past, and are characterised by SFH that are much more self-similar than those of the highest redshift sources, which are still in the process of assembling and show a high level of stochasticity. Despite being dusty (Sect. 4.4), their assembly histories suggest that their high M/L indicate evolved stellar populations, which are already in place at these early cosmic times (see Sect. 4.2; Looser et al. 2024; Kuruvanthodi et al. 2024; Russell et al. 2025; Merlin et al. 2025; Baker et al. 2025). This result provides further evidence for the hypothesis that baryonic mass assembly might be occurring more rapidly than current galaxy formation and cosmological models predict (e.g., Liu & Bromm 2022; Menci et al. 2022; Dekel et al. 2023; Melia 2023; Padmanabhan & Loeb 2023).

The progenitors of evolved galaxies at $z \sim 7-8$ are expected to be luminous ($M_{UV} < -20$) at $z > 20$, i.e., during the epoch of their formation. Despite the rarity of these sources, which represent $\sim 1\%$ of our sample, finding bright candidates at extremely high redshift (as could be the case of Capotauro, Gandolfi et al. 2025b) should not be unexpected. We note, however, that we may expect the phase of major assembly of these galaxies to be dust enshrouded, causing a different SFR-to-UV luminosity conversion. Considering a conservative case, i.e. $\log K_{UV}^{\text{obs}} \sim -26$, corresponding to an E(B–V) of ~ 0.6 , only 22% of the sources

would exceed the -20 limit, but 74% of them would still be brighter than -17 , therefore within reach of our telescopes.

For reference, in Fig. E.1 we show the assembly histories of quiescent galaxies with $sSFR < 0.1 \text{ Gyr}^{-1}$. Some of them, typically the most massive ones, have formed their stars very early, and they did not experience significant SF over the past 500 Myr at least (red to light blue coloured curves). Conversely, the least massive ones recently underwent a phase of super-Eddington SF over the past 300 Myr (bluish curves), consistently with a downsizing scenario (Cowie et al. 1996; Fontanot et al. 2009) and qualitatively in agreement with the results of Merlin et al. (2025), therefore still host relatively young stellar populations. Examples of young stellar populations in galaxies with low current SF, i.e., experiencing bursty star formation, are also reported by Looser et al. (2025).

6. Summary and conclusions

We investigated the specific SFR ($sSFR$) and the stellar populations as traced by the mass-to-light ratio (M/L) in a sample of 2420 $z = 6.5 - 14.5$ galaxies carefully selected from the JWST-ASTRODEEP database adopting photometric and photo- z criteria. We modeled this sample assuming non-parametric SFHs and extensively tested the robustness of our results against systematics related with the SED fitting assumptions, in particular the choice of the SFH. After validating the inferred physical properties against spectroscopic measurements and assessing the robustness of stellar masses and $sSFR$ in the absence of optical constraints at $z \gtrsim 10$, we obtained the following results.

- The $sSFR$ of the bulk of the population shows no evidence of evolution with cosmic time at $z > 6$, as indicated by the flat median trend across the redshift range probed.
- We measured a non-evolving relation between the stellar mass and the rest-frame UV luminosity in three redshift bins, with a large scatter of more than two orders of magnitude in mass at a given luminosity.
- The mass-to-light ratio spans up to four orders of magnitude at $z \sim 7$ and a factor of ~ 50 at $z > 10$, indicating a wide diversity in galaxy stellar populations, and its median shows no evolution with cosmic time.
- We identified distinct galaxy populations: star-forming systems with moderate ($E(B-V) < 0.2$) dust attenuation observed across the full redshift range; more heavily obscured ($E(B-V) \sim 0.2 - 0.7$) star-forming galaxies predominantly at $z \lesssim 9 - 10$; quiescent galaxies ($sSFR < 0.1 \text{ Gyr}^{-1}$) in place since $z \sim 10$. Remarkably, galaxies with high M/L , observed up to $z \sim 10$, include a mixture of the latter two populations.

None of the theoretical predictions analysed in this work can reproduce the observed diversity of physical properties, suggesting that a combination of mechanisms is required to explain the data. The evolutionary trends in our measurements shows qualitative agreement with the scenario of ‘feedback-free starburst’ combined with weak feedback at high- z implemented in the GAEA simulation (Cantarella et al. 2025), and are in contrast with the increasing trend of the $sSFR$ towards earlier epochs expected by the other models. This mismatch would however be explained by the presence of a population of intense star-forming, highly dust obscured galaxies hidden to our view. The existence of such population has been postulated by the Attenuation Free Model (AFM) of Ferrara (2024a) as a phase of major mass assembly preceding a radiation-driven outflow, clearing dust and gas. While the dusty phase would be out of reach with

current data, the so-called blue monster phase, immediately following the outflow and prior to the SF suppression, would not be captured by our observations likely because of its short duty cycle at very high redshifts ($z > 12$).

Although we cannot observe $z > 10$ dusty galaxies with our data, we can attempt to corroborate their existence by indirect means. Tracing back the SFH and making assumptions on the SFR-to-UV luminosity ratio, we attempted to recover the assembly histories and observability of the progenitors of a few extreme classes of objects.

- The majority of the highest redshift ($z > 11$) galaxies have experienced a vigorous phase of SF shortly ($\lesssim 50 \text{ Myr}$) before the epoch of observation, consistently with the scenario depicted by the AFM. They have assembled over their past 150-300 Myr, with short and repeated episodes of intense SF activity. Their progenitors are expected to be on average faint in the rest-frame UV, even without invoking an extremely dust obscured phase.
- Galaxies with high M/L at $z \sim 7 - 8$ have assembled the bulk of their mass before $z \sim 20$, i.e., 500–800 Myr prior to observation, indicating the presence of already evolved stellar populations in the first few hundreds of Myr of our Universe. They do not descend from the highest redshift candidates known (e.g., $z \sim 14$), but their progenitors may be within reach of current observational facilities, with the majority expected to have a UV magnitude at $z > 20$ brighter than -20 or -17 , depending on the assumptions.
- The properties of quiescent galaxies depend on their stellar mass. The most massive systems did not undergo significant SF activity since $\sim 500 \text{ Myr}$, while lower mass ones formed the bulk of their stars more recently (over their past $\sim 300 \text{ Myr}$), and are likely experiencing ‘lulling’ phases in their SFH.

Synergy between long wavelength observations (with MIRI and ALMA) and large spectroscopic surveys are critical to validate the existence of significant amount of dust in high redshift systems and discriminate among the different models proposed to address the excess of UV-bright galaxies.

Acknowledgements. Some of the data products presented herein were retrieved from the Dawn JWST Archive (DJA). DJA is an initiative of the Cosmic Dawn Center (DAWN), which is funded by the Danish National Research Foundation under grant DNRF140. We acknowledge support from: INAF RF2024 Large Grant “UNDUST: UNveiling the Dawn of the Universe with JWST”; INAF RF2022 Mini Grant “The evolution of passive galaxies through cosmic time”; INAF RF2024 GO Grant “Revealing the nature of bright galaxies at cosmic dawn with deep JWST spectroscopy”; INAF RF2022 Large Grant “Extragalactic Surveys with JWST”; PRIN 2022 MUR project 2022CB3PJ3 “First Light And Galaxy Assembly” (FLAGS) funded by the European Union NextGenerationEU; PRIN-MIUR 2020SKSTHZ grant; INAF Grants “The Big-Data era of cluster lensing” and “Probing Dark Matter and Galaxy Formation in Galaxy Clusters through Strong Gravitational Lensing”. PB acknowledges financial support from the Italian Space Agency (ASI) through contract “Euclid - Phase E”.

References

- Adame, A. G., Aguilar, J., Ahlen, S., et al. 2025, *J. Cosmology Astropart. Phys.*, 2025, 021
- Álvarez-Márquez, J., Crespo Gómez, A., Colina, L., et al. 2025, *A&A*, 695, A250
- Arrabal Haro, P., Dickinson, M., Finkelstein, S. L., et al. 2023, *Nature*, 622, 707
- Bagley, M. B., Pirzkal, N., Finkelstein, S. L., et al. 2024, *ApJ*, 965, L6
- Baker, W. M., Valentino, F., Lagos, C. d. P., et al. 2025, *A&A*, 702, A270
- Barro, G., Pérez-González, P. G., Kocevski, D. D., et al. 2024, *ApJ*, 963, 128
- Bergamini, P., Acebron, A., Grillo, C., et al. 2023, *ApJ*, 952, 84
- Bezanson, R., Labbe, I., Whitaker, K. E., et al. 2024, *ApJ*, 974, 92

- Bhatawdekar, R., Conselice, C. J., Margalef-Bentabol, B., & Duncan, K. 2019, *MNRAS*, 486, 3805
- Boquien, M., Burgarella, D., Roehly, Y., et al. 2019, *A&A*, 622, A103
- Bruzual, G. & Charlot, S. 2003, *MNRAS*, 344, 1000
- Bunker, A. J., Saxena, A., Cameron, A. J., et al. 2023, *A&A*, 677, A88
- Calabrò, A., Pentericci, L., Santini, P., et al. 2024, *A&A*, 690, A290
- Calzetti, D., Armus, L., Bohlin, R. C., et al. 2000, *ApJ*, 533, 682
- Cameron, A. J., Saxena, A., Bunker, A. J., et al. 2023, *A&A*, 677, A115
- Cantarella, S., De Lucia, G., Fontanot, F., et al. 2025, arXiv e-prints, arXiv:2511.03787
- Carniani, S., D'Eugenio, F., Ji, X., et al. 2025, *A&A*, 696, A87
- Carniani, S., Hainline, K., D'Eugenio, F., et al. 2024, *Nature*, 633, 318
- Carvajal-Bohorquez, C., Ciesla, L., Laporte, N., et al. 2025, arXiv e-prints, arXiv:2507.13160
- Castellano, M., Fontana, A., Merlin, E., et al. 2025, *A&A*, accepted, arXiv:2504.05893
- Castellano, M., Fontana, A., Treu, T., et al. 2023, *ApJ*, 948, L14
- Castellano, M., Fontana, A., Treu, T., et al. 2022, *ApJ*, 938, L15
- Castellano, M., Napolitano, L., Fontana, A., et al. 2024, *ApJ*, 972, 143
- Castellano, M., Sommariva, V., Fontana, A., et al. 2014, *A&A*, 566, A19
- Chabrier, G. 2003, *ApJ*, 586, L133
- Ciesla, L., Elbaz, D., & Fensch, J. 2017, *A&A*, 608, A41
- Ciesla, L., Elbaz, D., Ilbert, O., et al. 2024, *A&A*, 686, A128
- Ciesla, L., Gómez-Guijarro, C., Buat, V., et al. 2023, *A&A*, 672, A191
- Cochrane, R. K., Katz, H., Begley, R., Hayward, C. C., & Best, P. N. 2025, *ApJ*, 978, L42
- Cole, J. W., Papovich, C., Finkelstein, S. L., et al. 2025, *ApJ*, 979, 193
- Conselice, C. J., Adams, N., Harvey, T., et al. 2025, *ApJ*, 983, 30
- Côté, B., Silvia, D. W., O'Shea, B. W., Smith, B., & Wise, J. H. 2018, *ApJ*, 859, 67
- Cowie, L. L., Songaila, A., Hu, E. M., & Cohen, J. G. 1996, *AJ*, 112, 839
- Curti, M., D'Eugenio, F., Carniani, S., et al. 2023, *MNRAS*, 518, 425
- Curtis-Lake, E., Carniani, S., Cameron, A., et al. 2023, *Nature Astronomy*, 7, 622
- Davé, R., Finlator, K., & Oppenheimer, B. D. 2011, *MNRAS*, 416, 1354
- de Graaff, A., Brammer, G., Weibel, A., et al. 2025, *A&A*, 697, A189
- De Lucia, G., Fontanot, F., Xie, L., & Hirschmann, M. 2024, *A&A*, 687, A68
- Dekel, A., Mandelker, N., Li, Z., et al. 2025, *MNRAS*, 544, 160
- Dekel, A., Sarkar, K. C., Birnboim, Y., Mandelker, N., & Li, Z. 2023, *MNRAS*, 523, 3201
- Dekel, A., Zolotov, A., Tweed, D., et al. 2013, *MNRAS*, 435, 999
- D'Eugenio, F., Maiolino, R., Carniani, S., et al. 2024, *A&A*, 689, A152
- Donnan, C. T., Dickinson, M., Taylor, A. J., et al. 2025, *ApJ*, 993, 224
- Donnan, C. T., McLeod, D. J., Dunlop, J. S., et al. 2023, *MNRAS*, 518, 6011
- Dotterini, D., Calabrò, A., Pentericci, L., et al. 2025, *A&A*, 698, A234
- Dressler, A., Rieke, M., Eisenstein, D., et al. 2024, *ApJ*, 964, 150
- Duncan, K., Conselice, C. J., Mortlock, A., et al. 2014, *MNRAS*, 444, 2960
- Eisenstein, D. J., Willott, C., Alberts, S., et al. 2023, arXiv e-prints, arXiv:2306.02465
- Endsley, R., Chisholm, J., Stark, D. P., Topping, M. W., & Whitler, L. 2025, *ApJ*, 987, 189
- Faucher-Giguère, C.-A. 2018, *MNRAS*, 473, 3717
- Ferrara, A. 2024a, *A&A*, 684, A207
- Ferrara, A. 2024b, *A&A*, 689, A310
- Ferrara, A., Pallottini, A., & Dayal, P. 2023, *MNRAS*, 522, 3986
- Finkelstein, S. L., Bagley, M. B., Arrabal Haro, P., et al. 2025, *ApJ*, 983, L4
- Finkelstein, S. L., Bagley, M. B., Ferguson, H. C., et al. 2023, *ApJ*, 946, L13
- Finkelstein, S. L., Leung, G. C. K., Bagley, M. B., et al. 2024, *ApJ*, 969, L2
- Fontana, A., D'Odorico, S., Poli, F., et al. 2000, *AJ*, 120, 2206
- Fontanot, F., De Lucia, G., Monaco, P., Somerville, R. S., & Santini, P. 2009, *MNRAS*, 397, 1776
- Furlanetto, S. R. & Mirocha, J. 2022, *MNRAS*, 511, 3895
- Gandolfi, G., Rodighiero, G., Bisigello, L., et al. 2025a, arXiv e-prints, arXiv:2502.02637
- Gandolfi, G., Rodighiero, G., Castellano, M., et al. 2025b, *A&A*, accepted, arXiv:2509.01664
- Gelli, V., Pallottini, A., Salvadori, S., et al. 2025, *ApJ*, 985, 126
- Hainline, K. N., D'Eugenio, F., Jakobsen, P., et al. 2024a, *ApJ*, 976, 160
- Hainline, K. N., Helton, J. M., Johnson, B. D., et al. 2024b, *ApJ*, 964, 66
- Harikane, Y., Inoue, A. K., Ellis, R. S., et al. 2025, *ApJ*, 980, 138
- Harikane, Y., Nakajima, K., Ouchi, M., et al. 2024, *ApJ*, 960, 56
- Harikane, Y., Ouchi, M., Oguri, M., et al. 2023a, *ApJS*, 265, 5
- Harikane, Y., Zhang, Y., Nakajima, K., et al. 2023b, *ApJ*, 959, 39
- Harvey, T., Conselice, C. J., Adams, N. J., et al. 2025, *ApJ*, 978, 89
- Haskell, P., Das, S., Smith, D. J. B., et al. 2024, *MNRAS*, 530, L7
- Hegde, S., Wyatt, M. M., & Furlanetto, S. R. 2024, *J. Cosmology Astropart. Phys.*, 2024, 025
- Heintz, K. E., Watson, D., Brammer, G., et al. 2024, *Science*, 384, 890
- Helton, J. M., Alberts, S., Rieke, G. H., et al. 2025a, arXiv e-prints, arXiv:2506.02099
- Helton, J. M., Rieke, G. H., Alberts, S., et al. 2025b, *Nature Astronomy*, 9, 729
- Holwerda, B. W., Hsu, C.-C., Hathi, N., et al. 2024, *MNRAS*, 529, 1067
- Hsiao, T. Y.-Y., Abdurro'uf, Coe, D., et al. 2024, *ApJ*, 973, 8
- Inayoshi, K., Harikane, Y., Inoue, A. K., Li, W., & Ho, L. C. 2022, *ApJ*, 938, L10
- Inoue, A. K. 2011, *MNRAS*, 415, 2920
- Kartaltepe, J. S., Rose, C., Vanderhoof, B. N., et al. 2023, *ApJ*, 946, L15
- Kikuchihiro, S., Ouchi, M., Ono, Y., et al. 2020, *ApJ*, 893, 60
- Kim, H., Kim, J.-h., Jung, M., et al. 2025, arXiv e-prints, arXiv:2511.04435
- Kocevski, D. D., Finkelstein, S. L., Barro, G., et al. 2025, *ApJ*, 986, 126
- Kokorev, V., Atek, H., Chisholm, J., et al. 2025a, *ApJ*, 983, L22
- Kokorev, V., Caputi, K. I., Greene, J. E., et al. 2024, *ApJ*, 968, 38
- Kokorev, V., Chávez Ortiz, O. A., Taylor, A. J., et al. 2025b, *ApJ*, 988, L10
- Kuruvanthodi, A., Schaerer, D., Marques-Chaves, R., et al. 2024, *A&A*, 691, A310
- Labbe, I., Greene, J. E., Bezanson, R., et al. 2025, *ApJ*, 978, 92
- Lee, J. H., Park, C., Hwang, H. S., & Kwon, M. 2024, *ApJ*, 966, 113
- Leethochawalit, N., Trenti, M., Santini, P., et al. 2023, *ApJ*, 942, L26
- Leja, J., Carnall, A. C., Johnson, B. D., Conroy, C., & Speagle, J. S. 2019, *ApJ*, 876, 3
- Leja, J., Speagle, J. S., Ting, Y.-S., et al. 2022, *ApJ*, 936, 165
- Liu, B. & Bromm, V. 2022, *ApJ*, 937, L30
- Looser, T. J., D'Eugenio, F., Maiolino, R., et al. 2025, *A&A*, 697, A88
- Looser, T. J., D'Eugenio, F., Maiolino, R., et al. 2024, *Nature*, 629, 53
- Lower, S., Narayanan, D., Leja, J., et al. 2020, *ApJ*, 904, 33
- Mason, C. A., Trenti, M., & Treu, T. 2023, *MNRAS*, 521, 497
- McClymont, W., Tacchella, S., Smith, A., et al. 2025, *MNRAS*, 544, 513
- McLeod, D. J., Donnan, C. T., McLure, R. J., et al. 2024, *MNRAS*, 527, 5004
- Melia, F. 2023, *MNRAS*, 521, L85
- Menci, N., Castellano, M., Santini, P., et al. 2022, *ApJ*, 938, L5
- Menci, N., Sen, A. A., & Castellano, M. 2024, *ApJ*, 976, 227
- Merlin, E., Fortuni, F., Calabrò, A., et al. 2025, *The Open Journal of Astrophysics*, 8, E170
- Merlin, E., Pilo, S., Fontana, A., et al. 2019, *A&A*, 622, A169
- Merlin, E., Santini, P., Paris, D., et al. 2024, *A&A*, 691, A240
- Mitsuhashi, I., Suess, K. A., Leja, J., et al. 2025, arXiv e-prints, arXiv:2510.13240
- Muratov, A. L., Kereš, D., Faucher-Giguère, C.-A., et al. 2015, *MNRAS*, 454, 2691
- Naidu, R. P., Oesch, P. A., Brammer, G., et al. 2025, arXiv e-prints, arXiv:2505.11263
- Naidu, R. P., Oesch, P. A., van Dokkum, P., et al. 2022, *ApJ*, 940, L14
- Nakazato, Y. & Ferrara, A. 2024, arXiv e-prints, arXiv:2412.07598
- Napolitano, L., Castellano, M., Pentericci, L., et al. 2025a, *A&A*, 693, A50
- Napolitano, L., Castellano, M., Pentericci, L., et al. 2025b, *ApJ*, 989, 75
- Napolitano, L., Pentericci, L., Dickinson, M., et al. 2025c, arXiv e-prints, arXiv:2508.14171
- Narayanan, D., Torrey, P., Stark, D., et al. 2025, arXiv e-prints, arXiv:2509.18266
- Oke, J. B. & Gunn, J. E. 1983, *ApJ*, 266, 713
- Osterbrock, D. E. 1989, *Astrophysics of gaseous nebulae and active galactic nuclei*
- Pacifici, C., Iyer, K. G., Mobasher, B., et al. 2023, *ApJ*, 944, 141
- Padmanabhan, H. & Loeb, A. 2023, *ApJ*, 953, L4
- Papovich, C., Dickinson, M., & Ferguson, H. C. 2001, *ApJ*, 559, 620
- Pérez-González, P. G., Barro, G., Rieke, G. H., et al. 2024, *ApJ*, 968, 4
- Pérez-González, P. G., Östlin, G., Costantin, L., et al. 2025, *ApJ*, 991, 179
- Planck Collaboration, Aghanim, N., Akrami, Y., et al. 2020, *A&A*, 641, A6
- Reddy, N. A., Topping, M. W., Shapley, A. E., et al. 2022, *ApJ*, 926, 31
- Roberts-Borsani, G., Bagley, M., Rojas-Ruiz, S., et al. 2025a, *ApJ*, 983, 18
- Roberts-Borsani, G., Oesch, P., Ellis, R., et al. 2025b, arXiv e-prints, arXiv:2508.21708
- Roberts-Borsani, G., Treu, T., Chen, W., et al. 2023, *Nature*, 618, 480
- Robertson, B. E., Tacchella, S., Johnson, B. D., et al. 2023, *Nature Astronomy*, 7, 611
- Rodighiero, G., Bisigello, L., Iani, E., et al. 2023, *MNRAS*, 518, L19
- Rojas-Ruiz, S., Bagley, M., Roberts-Borsani, G., et al. 2025, *ApJ*, 985, 80
- Russell, T. A., Dobric, N., Adams, N. J., et al. 2025, *MNRAS*[arXiv:2412.11861]
- Santini, P., Fontana, A., Castellano, M., et al. 2017, *ApJ*, 847, 76
- Santini, P., Fontana, A., Castellano, M., et al. 2023, *ApJ*, 942, L27
- Schaerer, D. & de Barros, S. 2009, *A&A*, 502, 423
- Schaerer, D., Marques-Chaves, R., Barrufet, L., et al. 2022, *A&A*, 665, L4
- Somerville, R. S. & Davé, R. 2015, *ARA&A*, 53, 51
- Somerville, R. S., Olsen, C., Yung, L. Y. A., et al. 2021, *MNRAS*, 502, 4858
- Somerville, R. S., Yung, L. Y. A., Lancaster, L., et al. 2025, *MNRAS*[arXiv:2505.05442]
- Song, M., Finkelstein, S. L., Ashby, M. L. N., et al. 2016, *ApJ*, 825, 5
- Stefanon, M., Bouwens, R. J., Labbé, I., et al. 2021, *ApJ*, 922, 29
- Tacchella, S., Johnson, B. D., Robertson, B. E., et al. 2023, *MNRAS*, 522, 6236
- Tang, M., Stark, D. P., Mason, C. A., et al. 2025, arXiv e-prints, arXiv:2507.08245
- Topping, M. W., Stark, D. P., Senchyna, P., et al. 2025, *ApJ*, 980, 225
- Treu, T., Calabrò, A., Castellano, M., et al. 2023, *ApJ*, 942, L28
- Treu, T., Roberts-Borsani, G., Bradac, M., et al. 2022, *ApJ*, 935, 110
- Trussler, J. A. A., Conselice, C. J., Adams, N., et al. 2025, *MNRAS*, 537, 3662
- Wang, B., Fujimoto, S., Labbé, I., et al. 2023, *ApJ*, 957, L34
- Wang, B., Leja, J., Atek, H., et al. 2025a, *ApJ*, 987, 184
- Wang, B., Leja, J., Atek, H., et al. 2024, *ApJ*, 963, 74
- Wang, T., Sun, H., Zhou, L., et al. 2025b, *ApJ*, 988, L35
- Weibel, A., de Graaff, A., Setton, D. J., et al. 2025, *ApJ*, 983, 11
- Whitler, L., Stark, D. P., Topping, M. W., et al. 2025, *ApJ*, 992, 63
- Witstok, J., Smit, R., Baker, W. M., et al. 2025, arXiv e-prints, arXiv:2507.22888
- Wu, Z., Eisenstein, D. J., Johnson, B. D., et al. 2025, *ApJ*, 992, 212
- Zavala, J. A., Castellano, M., Akins, H. B., et al. 2025, *Nature Astronomy*, 9, 155

Appendix A: Dependence on SED fitting assumptions

It is commonly known that the SED fitting assumptions may affect the inferred physical parameters (e.g., Pacifici et al. 2023; Wang et al. 2024; Harvey et al. 2025). This is particularly true for the choice of the SFH (e.g., Ciesla et al. 2017; Leja et al. 2019; Lower et al. 2020; Haskell et al. 2024). In order to verify that our main results are robust and independent of SED fitting systematics, we repeated the analysis with different assumptions.

First of all, we tested the effect of our parameter grid choice by *i*) decreasing the minimum age to 50 Myr, *ii*) increasing the maximum $E(B-V)$ on the lines to 2, and *iii*) assuming the stellar metallicity to be 20%, $1\times$ and $2\times$ Solar. None of these changes affect the results. The only appreciable difference is obtained in case *iii*), where, due to the lack of the low metallicity templates, the sSFR shifts upwards by 0.15 dex on average at $z > 10$. This, however, does not change our conclusions.

We then tested different assumptions for the SFH. In addition to our reference model *a*), i.e., non-parametric model, with linearly spaced time binning, $t_0 = 20$ Myr and flat prior, we considered the following cases:

b) same assumptions as *a*), but fixing the latest bin duration t_0 to 10 Myr;

c) same as *a*) but with log spaced time binning;

d) non-parametric model similar to *a*) but adopting a bursty-continuity prior (e.g., Leja et al. 2019), which avoids sharp variations in the SFH and is thought to be less prone to the outshining effect (Wang et al. 2025a);

e) same as *d*) but with log spaced time binning (Ciesla et al. 2023);

f) a parametric delayed SFH (see Eqn. 4 of Boquien et al. 2019) characterised by $\tau_{main} = 10, 100, 500, 1000$ Myr, plus a recent burst having $\tau_{burst} = 10, 25, 50$ Myr and $\text{age}_{burst} = 5, 10, 50$ Myr, with the mass fraction produced in the recent burst ranging from 0 to 60% (7 linearly spaced steps); in this case, we consider the SFR averaged over the last 10 Myr;

g) a parametric delayed SFH as in *f*), but the flexibility is accounted for by a recent period of constant SFR (Ciesla et al. 2017), lasting for 10, 50 or 100 Myr, which is a factor of r_{SFR} larger or lower than the SFR immediately before the constant phase, with $r_{SFR} = 0.1, 1, 5, 10, 50, 100$; again, we consider the SFR averaged over the last 10 Myr.

In the top panel of Fig. A.1 we show the evolution of the median sSFR for $10^8 - 10^9 M_\odot$ galaxies under the different assumptions described above. Overall, non-parametric fits have higher level of scatter, as expected since they aim at reproducing a broader variety of sources. Moreover, larger errors are expected when using non-parametric models compared to parametric ones, as the latter a priori rule out a significant fraction of possibilities (Leja et al. 2019; Haskell et al. 2024). Additionally, non-parametric fits show on average lower sSFR, with the various setups spanning 0.7 dex range for the highest redshift sources. This is likely a consequence of mitigation of the outshining effect, responsible for underestimating stellar masses (Papovich et al. 2001; Leja et al. 2022). While investigating in detail the origin of the differences among fits is beyond the scope of the present work, all of them consistently predict a flattening or decreasing trend at $z \gtrsim 8 - 9$, corroborating the robustness of our result.

A similar conclusion can be drawn for the M/L evolution, shown in the lower panel. The difference among the various setups is lower in this case (0.3 dex at the highest redshifts), which is again not unexpected, as the rest-frame UV luminosity is a

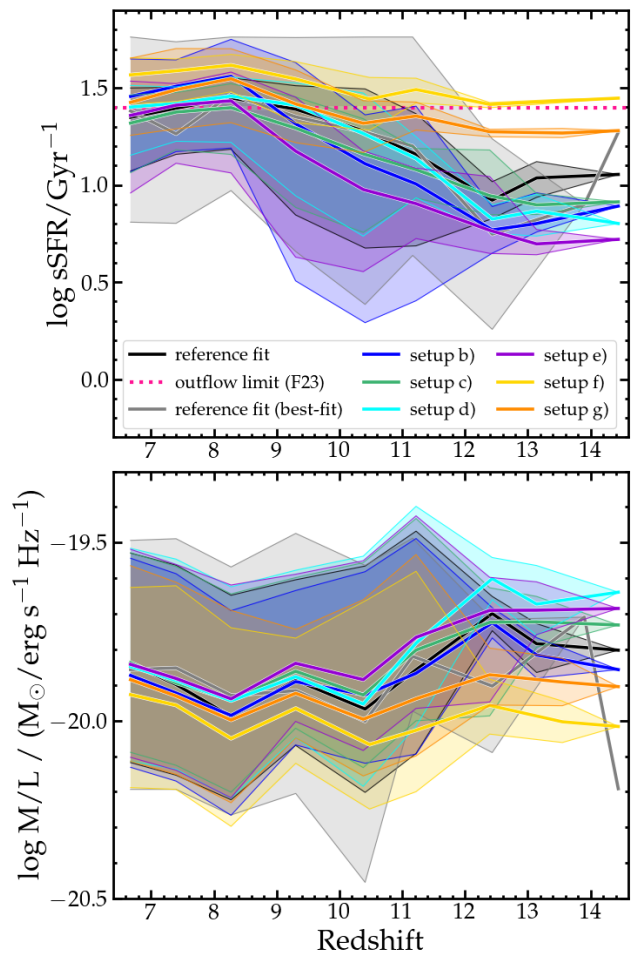


Fig. A.1. Median (solid lines) and 16th-84th percentile range (shaded areas) of the specific SFR (*top* panel) and M/L (*bottom* panel) vs redshift for $8 \leq \log(M/M_\odot) < 9$ galaxies according to different SED fitting assumptions and methodologies, as detailed in the legend.

much more stable parameter than the SFR, which is more affected by different SFH assumptions and dust attenuation.

Finally, we also tested that our results are robust against the methodology: if the best-fit solution is adopted instead of the median of the probability distribution function, results are overall unchanged, despite a larger scatter in the relations, as can be seen in Fig. A.1. Indeed, the adoption of the median value filters out outliers caused by extreme models.

Appendix B: Accuracy of the inferred physical properties

To verify the accuracy of the inferred SFR, we first compared our estimates to those inferred from emission lines for the spectroscopic sample of Dottorini et al. (2025), made of NIRSPEC sources extracted from the DJA archive. The common sample counts 680 sources.

We calculated the spectroscopic SFR following Calabrò et al. (2024). Briefly, we computed the gas phase attenuation either from the $H\alpha/H\beta$ Balmer decrement or from the SED fitting ($A_V = 4.05 \times E(B-V)_{\text{line}}$) in case only one line is available, and we calculated the dust-corrected $H\alpha$ luminosity. For galaxies

lacking $H\alpha$, we estimated its intrinsic luminosity from the dust-corrected $H\beta$, rescaled assuming an intrinsic $H\alpha/H\beta$ ratio of 2.86 (Osterbrock 1989). We then converted the $H\alpha$ luminosity into a SFR estimate adopting the calibration of Reddy et al. (2022), more appropriate for sub-Solar metallicity galaxies, typical at $z > 7$.

The comparison between SFRs calculated from SED fitting and those derived from spectroscopy is shown in the upper panel of Fig. B.1. While individual galaxies can differ by more than a factor of 10, the median offset in the logarithmic space is very close to zero, with a maximum deviation of ~ 0.2 dex in the 8.25–8.75 redshift bin.

Once the reliability of SED fitting as an SFR tracer has been verified, another potential issue affecting our results lies in the fact that the available photometry samples the optical rest-frame only up to $z \sim 10$, where the F444W filter encompasses the 4000Å break. At higher redshift, the rest-frame optical SED is unconstrained. To test whether this introduces any systematics in the estimated stellar masses and sSFR, we repeated the fit for the full sample by ignoring any filter redder than the F356W, i.e. the F410M and F444W filters. This setup mimics the absence of optical constraints suffered by $z \sim 10 - 14$ galaxies in the $z \sim 8 - 11$ redshift range. Indeed, the F444W filter extends up to rest-frame ~ 4500 (3300) Å at $z \sim 10$ (14), while the F356W filter probes up to ~ 4400 (3300) Å at $z \sim 8$ (11).

Although mass uncertainties increase, with relative uncertainties being on average $\sim 15\%$ higher and reaching $\sim 50\%$ at $z \sim 10$, the mean stellar masses are only mildly affected. Indeed, the ratio between the stellar mass inferred without rest-frame optical bands and those calculated exploiting the full photometry is always very close to unity, as shown by the second row panel of Fig. B.1. In the range of interest ($z \sim 8 - 11$, highlighted in light blue in the figure), the median offset is ~ 0.1 dex, well within the typical uncertainties on stellar masses. We can conclude that for the vast majority of galaxies the lack of the reddest filters does not affect the stellar mass estimates significantly, qualitatively in agreement with the results of Helton et al. (2025a), who tested the effect of MIRI photometry on the inferred physical parameters of $z \sim 8$ galaxies (but see also divergent results from Wang et al. 2025b and Cochrane et al. 2025). We note however that the distribution is highly asymmetric at specific redshifts, with a subset of sources in the tail of the distribution showing differences as large as a factor of 5 – 10. This occurs when the two reddest filters encompass the $H\beta$ and [OIII] lines (i.e. at $z \sim 8$), and the full set of filters allows the SED modeling to properly constrain nebular emission in these galaxies. Indeed, we verified that the sources whose stellar masses are substantially larger when the two reddest filters are excluded show high equivalent widths, and therefore lower stellar masses, when all bands are included in the fit. We note that this issue affects only a minority of sources, with only 2% of the total sample showing a difference larger than a factor of 5.

The third and bottom row panels of Fig. B.1 show a similar comparison for the sSFR and the mass-to-light ratio, respectively. An offset of ~ 0.1 dex in the opposite direction compared to the one for stellar mass is observed for the sSFR, suggesting that SFRs are not significantly affected by the lack of optical constraints. A similar conclusion can be drawn for the M/L, with an overall trend following the one shown by stellar masses, as expected.

For all three properties (M, sSFR, and M/L), the only significant deviation is observed at $z > 12$, although still within the typical uncertainties. However, deriving the properties of

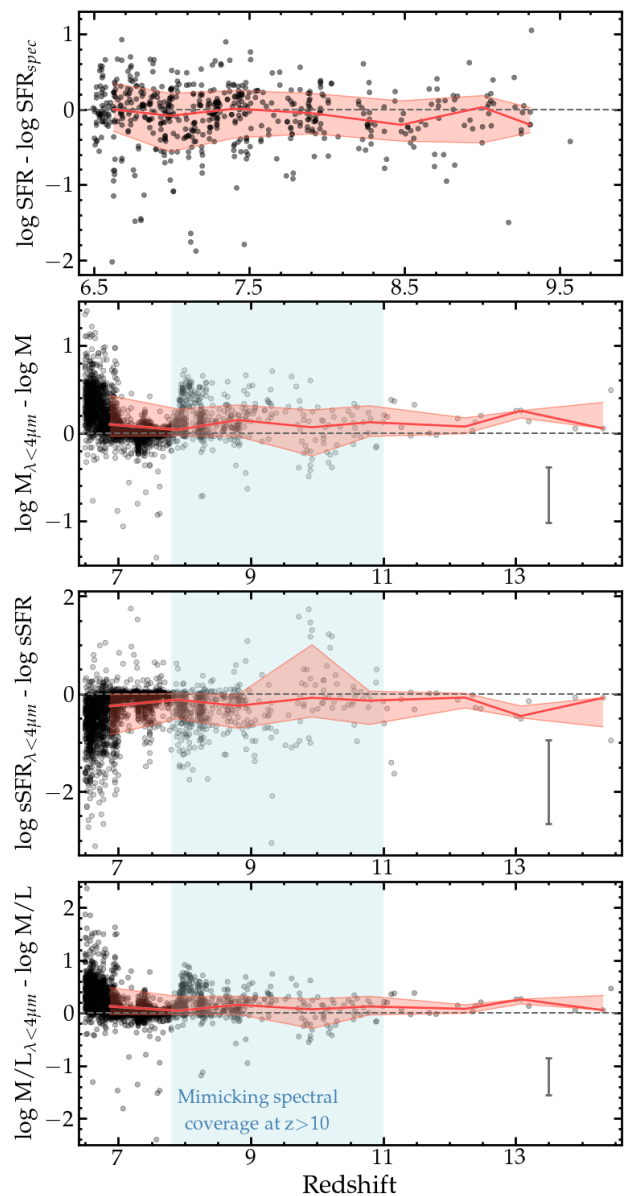


Fig. B.1. Upper panel: comparison of the SFR with spectroscopic values calculated from the sample of Dottorini et al. (2025). Other panels: comparison of the stellar mass (2nd row), sSFR (3rd row) and M/L (bottom row) with that inferred ignoring the two reddest filters, to mimic in the $z \sim 8 - 11$ range, shaded in light blue, the absence of rest-frame optical constraints affecting $z > 10$ galaxies. The error bar shows the median error obtained by symmetrizing and propagating the errors on the physical properties. In all panels, the red line and shaded area show the median and the 16th–84th percentiles range of all galaxies in bins of redshift.

$z \sim 12$ galaxies without the two reddest NIRCam filters is beyond our purposes, as it would simulate our ability to properly model galaxies outside the range of interest. Indeed, at this redshift the F356W filter samples the rest-frame region shortward of 2700Å, equivalently as the F444W filter does at $z \sim 15$.

In conclusion, the physical properties of galaxies in the critical $z \sim 8 - 11$ interval - where the spectral coverage without the two reddest filters matches that of our $z \sim 10 - 14$ sample - are

not affected by the lack of optical constraints, except for a small fraction of sources (a few percent), which does not impact the overall distribution.

Appendix C: Simulation to assess the selection window and completeness

As discussed in Sect. 3.2, given the complex selection criteria, we assessed the selection window and completeness of our sample using simulated galaxies.

We first considered the mock catalogs from the Santa Cruz semi-analytical model (SC-SAM hereafter, Somerville & Davé 2015; Somerville et al. 2021), and in particular the SC-SAM JWST deep-field model. We queried the FlatHUB⁵ archive and selected galaxies in the 6.5–15 redshift range with UV absolute magnitude (uncorrected for dust reddening) between -16.5 and -23.5 and stellar mass larger than $10^7 M_{\odot}$. Besides galaxy properties, the SC-SAM provides the expected photometry in the same bands used in this work with the exception of the HST WFC3 F140W band. We perturbed the predicted photometry according to the properties of the JADES-GS field, showcasing a compromise in terms of depth and area of the full dataset. We analyzed the mock photometry in the very same way as observed galaxies: we calculated the photometric redshifts and associated $P(z)$, inferred the physical properties, and applied the selections described in Sect. 2.2.

Most model galaxies are fainter than the observed ones, and the $\text{SNR} > 5$ cut in the F444W band is responsible for reducing the sample to 35%. The $z > 6.5$ threshold, the photometric cuts and the criteria based on the shape of the $P(z)$ further reduce the sample to 31, 28 and 22%, respectively. Overall, from an initial sample of 54122 mock galaxies we ended up with 11991 passing all selection criteria.

To evaluate the completeness of our selection, we considered bins of stellar masses, sSFR and UV luminosities at different redshifts. For each grid bin, we computed the ratio between the number of sources with the relevant inferred properties that pass the selection and the total number of input galaxies in the bin with the corresponding input properties. We report the results in Fig. C.1 (left panels).

As expected, the lowest completeness is found for low mass ($< 10^8 M_{\odot}$) and faint ($M_{UV} > -18$) galaxies, with less than 20–40% of galaxies recovered by the selection. Redshifts close to the lowest cut also suffer from a lower than average completeness level ($\sim 60 - 70\%$), due to galaxies being rejected as soon as they scatter below the threshold. The rest of the sample is highly complete in stellar mass and UV luminosity, typically $> 70 - 90\%$. The overall completeness in sSFR is quite low, but it is higher than 80–90% when limiting to galaxies in the mass range typical of observed sources, i.e., $8 \leq \log(M/M_{\odot}) < 9$ (central panels of Fig. C.1).

The distribution of stellar mass, UV luminosity and sSFR are well reproduced by our selection fitting procedure, especially when limiting to the typical mass range of our observed galaxies, including the increasing trend of the sSFR with redshift (bottom central panel of Fig. C.1).

The SC-SAM misses heavily dust-obscured objects and does not include dust at $z \gtrsim 10$ at all. To overcome this, we complemented it with galaxies simulated from stellar population synthesis models. We simulated galaxies with constant SFR, normalized to 10 and 100 M_{\odot}/yr , 10% Solar metallicity, age ranging from 20 Myr to the age of the Universe at the relevant redshift

and $E(B-V)$ equal to 0.7 or 1. Again, we perturbed their photometry and treated these mock galaxies in the very same way as the observed sample. As shown in the right panels of Fig. C.1, not unexpectedly, our selection is unable to select these galaxies, in particular at $z > 10$. Only 44% of the mock galaxies have the required significance ($> 5\sigma$) in the F444W band. The other steps of the selection, i.e., the $z > 6.5$ threshold, photometric cuts, and $P(z)$ constraints, progressively reduce the sample to 34, 24 and 10%, respectively, of its initial size. Moreover, for the few galaxies passing the selection criteria, the physical parameters are hardly reproduced, and the well-known degeneracy between red-dusty sources and red-passive ones is evident from the extremely low value recovered for their sSFR (bottom right panel). We note, however, that the observed quenched galaxies with $\text{sSFR} < 0.1/\text{Gyr}$ cannot be explained by this effect. Indeed, the expected M/L of simulated dusty galaxies erroneously fitted with low sSFR are extremely high, as a consequence of their extremely faint UV luminosity, whereas we do not recover similar M/L in our fits.

When only the $z > 10$ subsample is considered, the SED modeling lacks optical rest-frame constraints and relies on the rest-frame UV emission, most sensitive to dust obscuration. The fraction of $z > 10$ simulated galaxies passing this magnitude cut is only 21%. While the first two of the subsequent criteria reduce the sample to 14 and 9% of the parent sample, none of the sources passes the $P(z)$ selection, implying that their photometric redshift is never reliable enough to be considered in the final sample.

To conclude, our selection is significantly incomplete towards galaxies with a high level of dust obscuration, and it completely misses them at $z > 10$, where their existence has yet to be confirmed. Moreover, it suffers from severe incompleteness at stellar mass lower than $10^8 M_{\odot}$ and $M_{UV} > -18$. Our sample is instead reasonably complete at stellar masses between 10^8 and $10^9 M_{\odot}$, i.e. where the observed mass distribution peaks (see Fig. 2).

Appendix D: Best-fit of the mass-luminosity relations

We used linear least-squares regression to examine the relationship between the stellar mass and the rest-frame UV luminosity in different redshift bins. We parameterized the data as $\log M = a \cdot (M_{UV} + 19.5) + b$ and report the best-fit parameters in Table D.1.

Appendix E: Assembly history of the galaxies with low SF activity

We show in Fig. E.1 the assembly histories of galaxies with sSFR lower than 0.1/Gyr, discussed in Sect. 4.2 and 5.4.

⁵ <https://flathub.flatironinstitute.org>

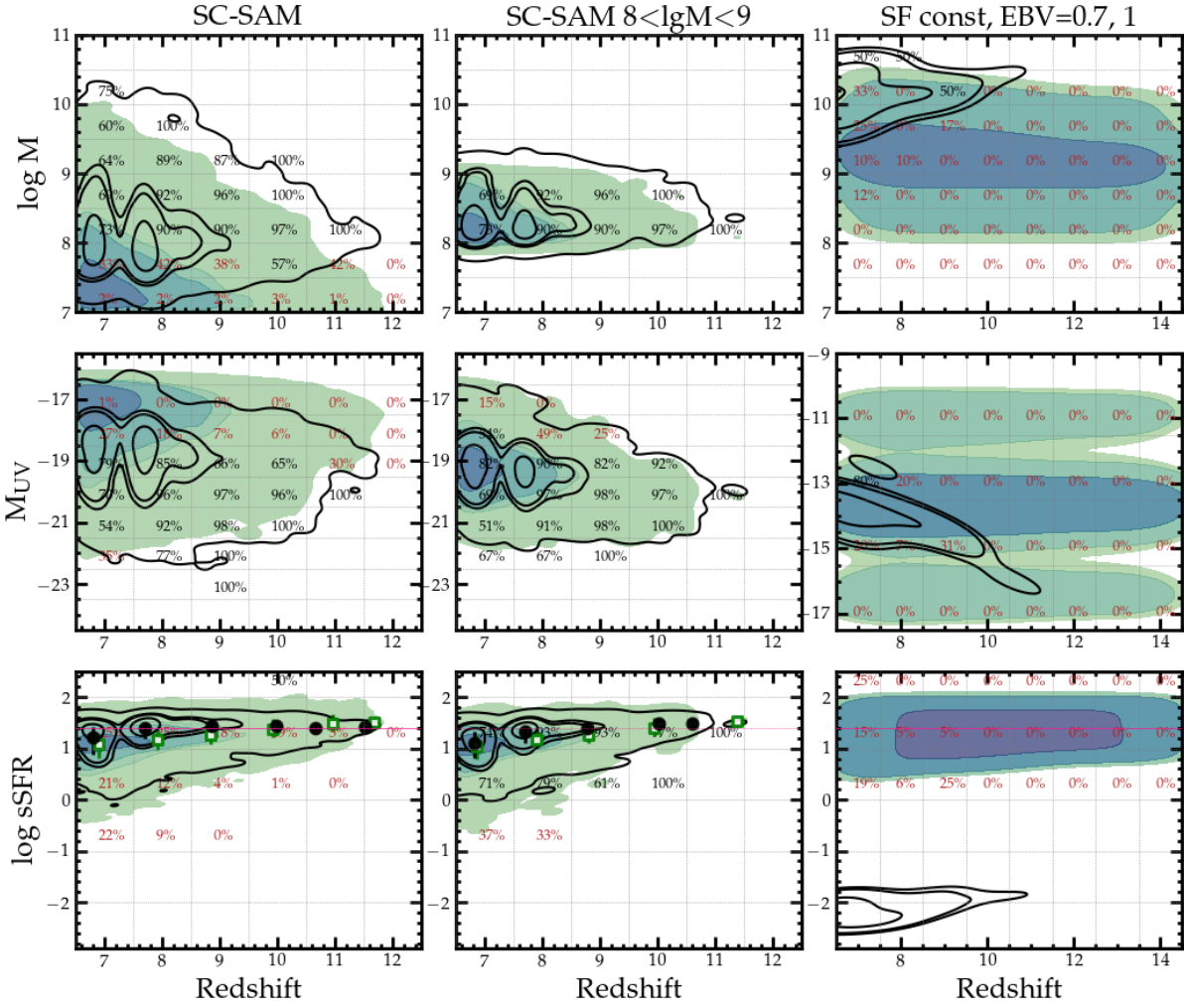


Fig. C.1. Coloured regions show the density of simulated galaxies (10, 40, 80 and 100%) at different redshifts and stellar masses (*top* panel), UV luminosities (*middle*) and sSFR (*bottom*). *Left* and *central* panels display galaxies from the SC-SAM with $\log(M/M_{\odot}) > 7$ and limited to the $8 \leq \log(M/M_{\odot}) < 9$ mass range, respectively, while the *right* panels represent simulated galaxies with constant SFR and heavily dust extinguished (note that the y-range in the central right panel is different, as such simulated galaxies are extremely faint at UV magnitudes). In each bin of the grid we report the fraction of sources recovered by our selection, with red labels indicating completeness lower than 50%. Black open contours show the distribution of inferred properties for the mock galaxies. In the bottom right and central panels, open green and solid black symbols show the median evolution of the sSFR considering the input properties and the inferred ones, respectively.

Redshift bin	a	b	Pearson coefficient
$6.5 \leq z < 7.5$	-0.37 ± 0.02	8.62 ± 0.01	-0.68
$7.5 \leq z < 9$	-0.28 ± 0.02	8.53 ± 0.02	-0.52
$9 \leq z < 14$	-0.35 ± 0.04	8.65 ± 0.04	-0.70

Table D.1. Best-fit parameters of the mass-luminosity relations, expressed as $\log M = a \cdot (M_{UV} + 19.5) + b$.

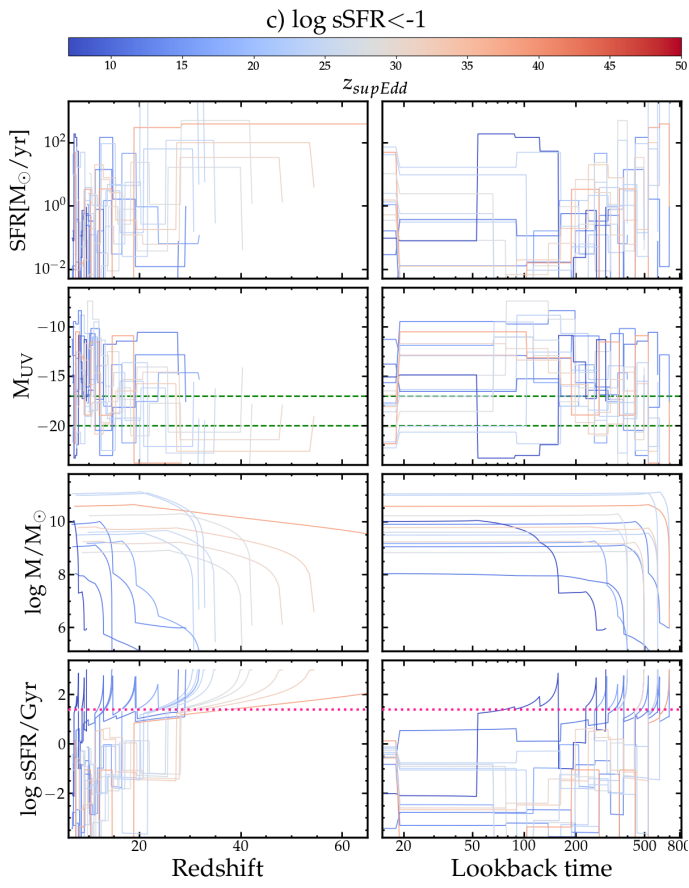


Fig. E.1. Same as Fig. 7, for galaxies with sSFR lower than $0.1/\text{Gyr}$.